**Naval Research Laboratory**
Washington, DC 20375-5320

# Temperature Histories of Structural Steel Laser and Hybrid Laser-GMA Welds Calculated Using Multiple Constraints

S.G. LAMBRAKOS

*Center for Computational Materials Science*
*Materials Science and Technology Division*

December 10, 2015

# REPORT DOCUMENTATION PAGE

| 1. REPORT DATE (DD-MM-YYYY)  10-12-2015 | 2. REPORT TYPE  NRL Memorandum Report | 3. DATES COVERED (From - To) |
|---|---|---|

**4. TITLE AND SUBTITLE**

Temperature Histories of Structural Steel Laser and Hybrid Laser-GMA Welds Calculated Using Multiple Constraints

**5a. CONTRACT NUMBER**

**5b. GRANT NUMBER**

**5c. PROGRAM ELEMENT NUMBER**

**6. AUTHOR(S)**

S.G. Lambrakos

**5d. PROJECT NUMBER**

**5e. TASK NUMBER**

**5f. WORK UNIT NUMBER**
63-4692-R5521

**7. PERFORMING ORGANIZATION NAME(S) AND ADDRESS(ES)**

Naval Research Laboratory, Code 6390
4555 Overlook Avenue, SW
Washington, DC 20375-5320

**8. PERFORMING ORGANIZATION REPORT NUMBER**

NRL/MR/6390--15-9665

**9. SPONSORING / MONITORING AGENCY NAME(S) AND ADDRESS(ES)**

Office of Naval Research
One Liberty Center
875 North Randolph Street, Suite 1425
Arlington, VA 22203-1995

**10. SPONSOR / MONITOR'S ACRONYM(S)**

ONR

**11. SPONSOR / MONITOR'S REPORT NUMBER(S)**

**12. DISTRIBUTION / AVAILABILITY STATEMENT**

Approved for public release; distribution is unlimited.

**13. SUPPLEMENTARY NOTES**

**14. ABSTRACT**

Inverse thermal analyses of structural steel deep-penetration welds are presented. These analyses employ a methodology that is in terms of numerical-analytical basis functions and multiple constraint conditions for inverse thermal analysis of steady state energy deposition in plate structures. These analyses provide parametric representations of weld temperature histories that can be adopted as input data to various types of computational procedures, such as those for prediction of solid-state phase transformations and mechanical response. In addition, these temperature histories can be used to construct parametric-function representations of thermal histories for welds corresponding to other process parameters or welding processes whose process conditions are within similar regimes. The present study applies an inverse thermal analysis procedure that uses volumetric constraint conditions whose two-dimensional projections are mappings onto transverse cross sections of experimentally measured solification boundaries and approximate edges of weld heat-affected zones.

**15. SUBJECT TERMS**

Inverse Thermal Analysis
Steel welds
Weld temperature histories

| 16. SECURITY CLASSIFICATION OF: | | | 17. LIMITATION OF ABSTRACT | 18. NUMBER OF PAGES | 19a. NAME OF RESPONSIBLE PERSON  Samuel G. Lambrakos |
|---|---|---|---|---|---|
| **a. REPORT**  Unclassified  Unlimited | **b. ABSTRACT**  Unclassified  Unlimited | **c. THIS PAGE**  Unclassified  Unlimited | Unclassified  Unlimited | 45 | **19b. TELEPHONE NUMBER** (include area code)  (202) 767-2601 |

Standard Form 298 (Rev. 8-98)
Prescribed by ANSI Std. Z39.18

# Contents

## Introduction

Inverse thermal analyses of structural steel deep-penetration welds are presented. These analyses provide a parameterization of temperature histories for prediction of properties within the Heat Affected Zone (HAZ) of welds for the regime considered. The present study applies an inverse thermal analysis procedure that uses volumetric constraint conditions whose two-dimensional projections are mappings onto transverse cross sections of experimentally measured solidification and transformation boundaries, or any type of specified boundary within the temperature field, including thermocouple measurements. For the present study, which considers deep-penetration welds of structural steel, experimentally observed solidification boundaries and approximate edges of the heat-affected zone (HAZ) are adopted as temperature-field constraint conditions. The inverse analyses presented in this study provide parametric representations of weld temperature histories that can be adopted as input data to computational procedures, such as those that predict solid-state phase transformations and mechanical response. In addition, these temperature-history parametric representations permit construction of a model-parameter space that can be adopted for inverse analysis of welds corresponding to other process parameters or welding processes whose process conditions are within similar regimes. The construction of temperature fields according to spatially and temporally distributed constraint conditions using linear combinations of basis functions, whose fundamental trend features are consistent with those of the underlying process, represents a convenient approach to inverse analysis of energy deposition processes. Finally, the results of this study contribute to a continually evolving database of weld cross sections and temperature histories corresponding to specified weld processes, process conditions and types of metals and their alloys.

The formal structure of the inverse analysis approach applied in this study is that of parametric model representation of the temperature field in terms of numerical-analytical basis functions. The foundation of this approach was introduced by [1], and provides a general reduction of model complexity for purposes of weld thermal analysis. Reduction of model complexity is achieved by adopting numerical-analytical models for either the heat source or temperature field (or both) in combination with numerical methods. Among notable studies applying this approach are [2-6]. The inverse analysis approach applied here has been used [7] for construction of a parameter space relating welding process parameters, e.g., current and welding speed, to weld efficiency for keyhole plasma arc welding. Similarly, the present study contributes to a parameter space relating shapes of weld solidification and transformation boundaries, or shapes any type of specified boundary within the temperature, to weld temperature histories, as well as to weld process parameters. A specific aspect of the inverse analysis methodology applied here, which permits convenient adjustment of parameters, is construction of discrete volumetric source distributions. This aspect of the methodology, although employing three-dimensional source distributions, is formally equivalent to the Myhr-Grong method [4], which typically employs discrete source distributions within two-dimensional planes transverse to the relative motion of heat source and workpiece. References [8,9], and reference therein, demonstrate the use of discrete source distributions for numerical modeling of transport phenomena associated with welding processes.

The mathematical foundation of the inverse analysis methodology for calculation of temperature histories using linear combinations of numerical-analytical basis functions is that of least-squares parameter optimization [10-13]. As discussed previously [10-15], the inverse modeling approach compensates for lack of information concerning material properties [14-20].

_____

This fundamental property of inverse models has been discussed and demonstrated previously [21-23].

The organization of the subject areas presented are as follows. First, a brief description of the general procedure for inverse analysis of heat deposition processes is presented. Second, results of inverse thermal analyses of structural steel deep penetration welds are presented. These results provide a quantitative parametric representation of temperature histories for these welds and for any welds associated with similar welding process conditions. Third, a discussion is presented concerning aspects of the inverse analysis procedure. Finally, a conclusion is given.

## Inverse Analysis Procedure

Following the inverse analysis approach [14-20], a parametric model provides a means for the inclusion of information concerning the physical characteristics of a given energy deposition process. Given the general trend features of temperature fields associated with welding processes, a consistent parametric representation of the temperature field for heat deposition within structures characterized by a finite thickness, in terms of numerical-analytical basis functions, is

$$T(\hat{x},t) = T_A + \sum_{k=1}^{N_k} \sum_{n=1}^{N_t} C(\hat{x}_k) G(\hat{x},\hat{x}_k,\kappa,n\Delta t,V) \tag{Eq 1a}$$

and

$$T(\hat{x}_n^c,t_n^c) = T_n^c, \tag{Eq 1b}$$

where

$$G(\hat{x},\hat{x}_k,t,\kappa,V) = \frac{1}{t}\exp\left[-\frac{(x-x_k-Vt)^2+(y-y_k)^2}{4\kappa t}\right]$$

$$\times\left\{1+2\sum_{m=1}^{\infty}\exp\left[-\frac{\kappa m^2\pi^2 t}{l^2}\right]\cos\left[\frac{m\pi z}{l}\right]\cos\left[\frac{m\pi z_k}{l}\right]\right\} \tag{Eq 2}$$

and

$$C(\hat{x}) = \sum_{k=1}^{N_k} Q(\hat{x}_k)\delta(\hat{x}-\hat{x}_k). \tag{Eq 3}$$

where $Q(\hat{x}_k)$ is the value of the discrete source function at location $\hat{x}_k$. The quantities $\kappa$, $V$ and $l$ are the thermal diffusivity, welding speed and plate thickness, respectively. The procedure for inverse analysis defined by Eqs.(1)-(3) entails adjustment of the parameters $C(\hat{x}_k)$, $\hat{x}_k$ and $\Delta t$ defined over the entire spatial region of the workpiece. Formally, this procedure entails adjustment of the steady state temperature field defined over the entire spatial region of the sample volume. This approach defines an optimization procedure where the temperature field spanning the spatial region of the sample volume is adopted as the quantity to be optimized. The constraint conditions are imposed on the temperature field spanning the bounded spatial domain of the workpiece by minimization of the value of the objective functions defined by

$$Z_T = \sum_{n=1}^{N} w_n\left(T(\hat{x}_n^c,t_n^c)-T_n^c\right)^2 \tag{Eq 4}$$

where $T_n^c$ is the target temperature for position $\hat{x}_n^c = (x_n^c, y_n^c, z_n^c)$. The quantities $w_n$ $(n=1,...,N)$ are weight coefficients that specify relative levels of influence associated with constraint conditions $T_n^c$.

The inverse analysis methodology defined by Eqs.(1)-(4) is based on a parametric numerical-analytical model, which combines numerical integration with optimization of linear combinations of numerical-analytical basis functions, which include fundamental solutions to the heat conduction equation [24] and their Fourier-series representation. In particular, Eq.(1a) defines a discrete numerical integration over time, where the time step $\Delta t$ is specified according to the average energy deposited during the time $\Delta t$, for transition of the temperature field to steady state. It should be noted that the formulation of the inverse analysis methodology defined by Eq.(1)-(4) is equipped with a mathematical structure that satisfies all boundary conditions associated with welding of plate structures (see [25] for further discussion).

In addition to the parameters defined with respect to Eqs.(1)-(4), the parameteric model applied for inverse analysis includes a length scale parameter $l_S$, where in general $l_S < l$ defined by Eq.(2), for specification of the spatial scale of the calculated temperature field with respect to which parameters are adjusted. This length scale parameter provides for inclusion of more details of shape features of measured solidification boundaries to be adopted as constraint conditions. However, for the analyses that follow, the two length parameters, i.e., the plate thickness $l$ and the depth $l_S$ of the speciifed region of the temperature field to be calculated, are taken to be the same.

### Inverse Thermal Analysis of Structural Steel Laser and Hybrid Laser-GMAWelds

In this section results of inverse thermal analyses of structural steel deep-penetration welds are described, which correspond to different weld process conditions and associated process-control parameters. The significance of the inverse-problem approach for these analyses is that the nature of the coupling of the energy source to the workpiece, which is a function of beam power and process control parameters, is in principle difficult to specify relative to analysis based on the direct-problem approach.

Previous studies considered inverse thermal analysis of steel welds using single cross section [25] and volumetric [26] constraint conditions. A series of studies [27-29] considered inverse thermal analysis of welds using multiple constraint conditions, where both solidification and phase-transformation boundaries were adopted as constraint conditions. In particular, welds of CP-Ti and a Ti-6Al-4V were considered [30-32], where weld-cross-section measurements of both solidifcation and estimated $\alpha - \beta$ phase-transformation boundaries were adopted as constraint conditions on the calculated temperature field. In these studies, motivation for adopting $\alpha - \beta$ phase transformation boundaries as constraint conditions was that in practice, for welds of Ti and its alloys, one can associate (approximately) this boundary with the observed edge of the HAZ, and accordingly, specify an isothermal boundary of known temperature. The present study is based on a similar motivation. In particular, for steel welds, especially those of structural steel, the HAZ consists by various regions whose microstructures have been well characterized (see reference [33] for further discussion). These regions are described schematically in Fig. 1. Referring to this figure, it should be noted that, for purposes of inverse thermal analysis, one should be able to associated the observed edge of the HAZ (approximately) with a maximum temperature 700 $^o$C. As discussed in reference [27], for regions within the workpiece not close to the energy source, reasonable estimates of temprature-field values, at specified locations, are sufficient for imposing constraint conditions.

3

The structural steel deep-penetration welds, whose inverse analysis is presented here, consist of laser and laser-GMA hybrid welds [34]. The analyses presented here entail calculation of the steady state temperature field for a specified range of sizes and shapes of inner surface boundaries $S_i$ defined by the solidification boundary and experimentally observed estimate of the HAZ edge. The shapes of these boundaries are determined experimentally by analysis of transverse weld cross sections showing microstructure revealing solidification and estimated HAZ-edge boundaries. For calculations adopting the solidification boundaries as constraints, the parameter values assumed are $\kappa = 5.88$ x $10^{-6}$ m$^2$s$^{-1}$, $T_M = 1503.0$ $^o$C. For calculations adopting the HAZ-edge boundaries as constraints, the parameter values assumed are $\kappa = 5.88$ x $10^{-6}$ m$^2$s$^{-1}$, $T_{HE} = 700$ $^o$C. As discussed previously [25, 27], reasonable estimates of $\kappa$ and $T_M$ are sufficient for inverse analysis. For this study, the same thermal diffusivity is assumed for calculation of temperature fields using solidification and estimated HAZ-edge constraints. This assumption is sufficient, within reasonable estimates, in that the set of parameters $C(\hat{x}_k)$, $k=1,...,N_k$, and $\kappa$ are not uniquely determined by inverse analysis. Thus, changing estimated values of $\kappa$ would require different values of $C(\hat{x}_k)$ in order to satisfy specified constraint conditions associated with $T_M$ and $T_{HE}$,. With respect to inverse analysis, the interpretation of $\kappa$ as both an estimated material property and adjustable parameter is emphasized within the following.

The goal of the present analysis is determination of a set of parameters that can serve as initial estimates for parameter adjustment with respect to deep penetration welds of steels, whose process parameters are within similar regimes. Parameter adjustment with respect to other welds, which assume the results of this study as initial estimates, would adopt $\kappa$ and $T_M$ as adjustable parameters, as well as the discrete source function $C(\hat{x}_k)$. Values of the workpiece thickness $l$ and welding speed $V$ defined in Eq. (2) are given in the figures below. The upstream boundary constraints on the temperature field, $T_c = T_M$ and $T_c = T_{HE}$ for $(y_c,z_c)$ defined in Eq. (1b), are given in Table 1 for the solidification and HAZ-edge boundaries, respectively. Given in Tables 2 through 17 are values of the discrete source function that have been calculated according to the constraint conditions and weld process specifications given in Table 1. The relative location of each discrete source is specified according to Fig. 2. Shown in Figs. 3 through 42 are experimentally measured transverse weld cross sections of solidification and HAZ-edge boundaries [34], and different planer slices of the steady state temperature field that have been calculated according to the constraint conditions given in Table 1. Referring to the planer slices of the calculated temperature fields shown in these figures, it can be seen that all boundary conditions are satisfied, namely the condition $T(\hat{x},t) = T_M$ or $T(\hat{x},t) = T_{HE}$ at the solidification or HAZ-edge boundary, respectively, and $\nabla T \cdot \hat{n} = 0$ at surface boundaries, where $\hat{n}$ is normal to the surface.

## Discussion

The inverse analysis procedure entails calculating either a three-dimensional solidification or HAZ-edge boundary using experimentally measured constraint conditions, and the temperature field consistent with the isothermal surface associated with this boundary.

Shown in Figs. 4, 9, 14, 19, 24, 29, 34 and 39 are two-dimensional slices of the calculated three-dimensional temperature field obtained using the constraint conditions given in Table 1 for the measured solidification boundary, which are parallel to the relative motion of laser or laser-GMA source and workpiece. Shown in Figs. 5, 10, 15, 20, 25, 30, 35 and 40 are two-dimensional slices of this three-dimensional temperature field that are perpendicular to the relative motion of laser or laser-GMA source and workpiece. Referring to these figures, it should be noted that $t = 0$ has been assigned arbitrarily to a two-dimensional slice at the leading edge of the solidification

boundary. Accordingly, shown in Figs. 5, 10, 15, 20, 25, 30, 35 and 40 is passage with time of the calculated three-dimensional solidification boundaries through experimentally measured transverse cross sections of these boundaries.

Shown in Figs. 6, 11, 16, 21, 26, 31, 36 and 41 are two-dimensional slices of the calculated three-dimensional temperature field obtained using the constraint conditions given in Tables 1 through 4 for the estimated HAZ-edge boundary, which are parallel to the relative motion of laser or laser-GMA source and workpiece. Shown in Figs. 7, 12, 17, 22, 27, 32, 37 and 42 are two-dimensional slices of this three-dimensional temperature field that are perpendicular to the relative motion of laser or laser-GMA source and workpiece. Again, referring to these figures, it should be noted that $t = 0$ has been assigned arbitrarily to a two-dimensional slice at the leading edge of the solidification boundary. Again, accordingly, shown in Figs. 7, 12, 17, 22, 27, 32, 37 and 42 is passage with time of the calculated three-dimensional solidification boundaries through experimentally measured transverse cross sections of these boundaries.

Referring to the calculated temperature fields shown above, it is important to note that the constraint conditions on the calculated three-dimensional solidification and HAZ-edge boundaries are that the projections of all their two-dimenional transverse slices, as a function of time, are consistent with the experimentally measured transverse cross sections of the solidification and transformation boundaries, respectively.

The final stage of the analysis entails calculation of temperature histories as a function of transverse position within the cross section of the weld. This is accomplished by constructing a steady state three-dimensional temperature field that is consistent with experimentally measured constraint conditions for the solidification boundary or for both solidification and HAZ-edge boundaries. In cases where both the solidification and HAZ-edge boundaries are adopted as constraints, this construction combines two regions of the temperature field. One region consists of the calculated temperature field obtained using HAZ-edge boundary constraints for all temperatures less than and equal to the temperature $T_{HE}$. The other region consists of the temperature field that is obtained by three-dimensional interpolation between isothermal surfaces $T_M$ and $T_{HE}$, which are associated with the solidification and HAZ-edge boundaries, respectively. In general, the numerical procedure for interpolation between constrained isotherms is a separate issue for consideration.

## Conclusion

A specific objective of this report is to further examine, for the case of structural steel welds, the concept of using HAZ-edge boundary constraints for inverse thermal analysis. This concept was introduced previously for inverse thermal analysis of CP-Ti and a Ti-6Al-4V welds [30-32]. A general objective of this report is to describe a quantitative inverse thermal analysis of structural steel deep-penetration welds corresponding to various weld process parameters and to construct numerical-analytical basis functions that can be used by weld analyst to calculated weld temperature histories, which are for welding processes associated with similar process conditions. This report contributes to the continuing evolution of a parametric representation of the temperature field $T(\hat{x}, t, \kappa, V, S_i, l)$ for inverse thermal analysis of welds associated with different types of metals, their alloys and weld process conditions. The weld temperature histories obtained by inverse analysis could in practice be used to predict solid- state phase transitions and mechanical response characteristics associated with temperature histories within localized spatial regions, and thus with evolution of plastic and elastic strains, resulting in distortion and residual stresses.

## Acknowledgement

## References

1. D. Rosenthal, "The theory of moving sources of heat and its application to metal treatments," Trans ASME, Vol. 68 (1946), pp. 849-866.

2  J. Goldak, A. Chakravarti and M. Bibby, "A new finite element model for welding heat source," Metall. Trans. B, Vol. 15, pp. 299-305, 1984.

3. O. Grong, "Metallurgical Modelling of Welding," 2ed., Materials Modelling Series, (H.K.D.H. Bhadeshia, ed.), published by The Institute of Materials, UK, (1997), chapter 2: pp. 1-115.

4. R.O. Myhr and O. Grong,'Acta Metall. Mater., 38, 1990, pp. 449-460.

5. R.C. Reed and H.K.D.H Bhadeshia: "A Simple Model For Multipass Welds," Acta Metall. Mater. 1994, 42(11), 3663-3678.

6. V.A. Karkhin, P.N. Homich and V.G. Michailov, "Models for Volume Heat Sources and Functional-Analytic Technique for Calculating the Temperature Fields in Butt Welding, 'Mathematical Modelling of Weld Phenomena,' Volume 8, 847, Published by Verlag der Technischen Universite Graz, Austria (2007).

7. A.A. Deshpande, A. Short, W. Sun, D.G. McCartney, L. Xu and T.H. Hyde, "Finite-Element Analysis of Experimentally Identified Parametric Envelopes for Stable Kethole Plasma Arc Welding of a Titanium Alloy," Journal of Strain Analysis for Engineering Design, 47(5), pp. 266-275, 2012.

8. I.S. Leoveanu, G. Zgura, D. Birsan, "Modeling the Heat and Fluid Flow in the Welded Pool," Bulletin of the Transsilvania University of Brasov, Vol. 3, pp. 363-368, ISSN 1223-9631, 2007.

9. I.S. Leoveanu and G. Zgura, "Modelling the Heat and Fluid Flow in the Welded Pool from High Power Arc Sources," Materials Science Forum, Editors: C. Lee, J-B. Lee, D-H. Park, S-J. Na, Vols. 580-582, pp.443-446, 2008.

10. R.W. Farebrother, Linear-Least-Square
 Computations, Marcel Dekker, New York, 1988.

11. Y.B. Bard, Nonlinear Parameter Estimation, Academic Press, New York. 1974.

12. K. Levenberg, "A Method for the Solution of Certain Non-linear Problems in Least-Squares", Quart. Appl. Math, 2, 164-168, 1944.

13. D.W. Marquardt, "An Algorithm for Least Squares Estimation of Nonlinear Parameters", J. Soc. Ind. Appl. Moth, II, 431-441, 1963.

14. A. Tarantola, "Inverse Problem Theory and Methods for Model Parameter Estimation," SIAM, Philadelphia, PA, 2005.

15. M.N. Ozisik and H.R.B. Orlande: Inverse Heat   Transfer, Fundamentals and Applications, Taylor and  Francis, New York, 2000.

16. K. Kurpisz and A.J. Nowak: Inverse Thermal Problems, Computational Mechanics Publications, Boston, USA, 1995.

17. O.M. Alifanov, Inverse Heat Transfer Problems.      Springer, Berlin, 1994.

18. J.V. Beck, B. Blackwell, C.R. St. Clair, Inverse Heat Conduction: Ill-Posed Problems, Wiley Interscience, New York, 1985.

19. J.V. Beck, "Inverse Problems in Heat Transfer with Application to Solidification and Welding," Modeling of Casting, Welding and Advanced Solidification Processes V, M. Rappaz,

M.R. Ozgu and K.W. Mahin eds., The Minerals, Metals and Materials Society, 1991, pp. 427-437.

20. J.V. Beck, "Inverse Problems in Heat Transfer," Mathematics of Heat Transfer, G.E. Tupholme and A.S. Wood eds., Clarendon Press, (1998), pp. 13-24.

21. S.G. Lambrakos and S.G. Michopoulos, Algorithms for Inverse Analysis of Heat Deposition Processes, 'Mathematical Modelling of Weld Phenomena,' Volume 8, 847, Published by Verlag der Technischen Universite Graz, Austria (2007).

22. S.G. Lambrakos and J.O. Milewski, Analysis of Welding and Heat Deposition Processes using an Inverse-Problem Approach, Mathematical Modelling of Weld Phenomena, **7**, 1025, Publishied by Verlag der Technischen Universite Graz, Austria 2005, pp. 1025-1055.

23. E.A. Metzbower, D.W. Moon, C.R. Feng, S.G. Lambrakos and R.J. Wong: "Modelling of HSLA-65 GMAW Welds," *Mathematical Modelling of Weld Phenomena*, **7**, Publishied by Verlag der Technischen Universite Graz, Austria, pp. 327-339 (2005).

24. H. S. Carslaw and J. C. Jaegar: Conduction of Heat in Solids, Clarendon Press, Oxford, 2nd ed, 374, 1959.

25. S.G. Lambrakos, "Inverse Thermal Analysis of 304L Stainless Steel Laser Welds," J. Mater. Eng. And Perform., 22(8), 2141 (2013).

26. S.G. Lambrakos, "Inverse Thermal Analysis of Stainless Steel Deep-Penetration Welds Using Volumetric Constraints," Journal of Materials Engineering and Performance, published online 2014, DOI: 10.1007/s11665-014-1023-7, Volume 23(6), June 2014, pp. 2219-2232.

27. S.G. Lambrakos, "Inverse Thermal Analysis of Welds Using Multiple Constraints and Relaxed Parameter Optimization," Journal of Materials Engineering and Performance, Volume 24(8) August 2015, pp. 2925-2936.

28. S.G. Lambrakos, A. Shabaev, L. Huang, "Inverse Thermal Analysis of Titanium GTA Welds Using Multiple Constraints," Journal of Materials Engineering and Performance, published online April 17, 2015, DOI: 10.1007/s11665-015-1511-4 , Volume 24(6), June 2015, pp. 2401-2411.

29. S.G. Lambrakos, A. Shabaev, "Temperature Histories of Ti-6Al-4V Pulsed-Mode Laser Welds Calculated Using Multiple Constraints," Naval Research Laboratory Memorandum Report, Naval Research Laboratory, Washington, DC, NRL/MR/6390--15-9621 (August 12, 2015).

30. R. Rai, P. Burgardt, J.O. Milewski, T.J. Lienert, T. DebRoy, "Heat Transfer and Fluid Flow During Electron Beam Welding of 21Cr-6Ni-9Mn steel and Ti-6AL-4V alloy," J. Phys. D: Appl. Phys. 42, 025503, 2009.

31. R. Rai, J.W. Elmer, T.A. Palmer, T. DebRoy, "Heat Transfer and Fluid Flow During Keyhole Mode Laser Welding of Tantalum, Ti-6AL-4V, 304L Stainless Steel and Vanadium," J. Phys. D: Appl. Phys. 40 5753-5766, 2007.

32. J.O. Milewski, Los Alamos National Laboratory (Ret.), private communication.

33. S. Kou, Welding Metallurgy, 2$^{nd}$ Ed., John Wiley & Sons, Inc.,  2003. DOI: 10.1002/0471434027.

34. J. K. Kristensen, "Laser and Hybrid Laser-GMA Welding of Structural Steels, A Challenge to Research and Industry for Two Decades," Trends in Welding Research, Proceedings of the 8th International Conference, Editors: S.A. David, T. DebRoy, J.N. DuPont, T. Koseki, H.B. Smartt, ASM International, 645-641, 2009.

35. B.D. Ribic, R. Rai, T.A. Palmer, T. DebRoy," Arc-Laser Interactions and Heat Transfer and Fluid Flow in Hybrid Welding," Trends in Welding Research, Proceedings of the 8th International Conference, Editors: S.A. David, T. DebRoy, J.N. DuPont, T. Koseki, H.B. Smartt, ASM International, 313-320, 2009.

36. E.W. Reutzel, S.M. Kelly, R.P. Martukanitz, M.M. Bugarewicz, P. Michaleris, "Laser-GMA Hybrid Welding: Process Monitoring and Thermal Modeling," Trends in Welding Research, Proceedings of the 7th International Conference, Editors: S.A. David, T. DebRoy, J.C. Lippold, H.B. Smartt, J.M. Vitek, ASM International, 143-148, 2006.

**Table 1** Temperature field constraint conditions at positions $(y_c, z_c)$ at solidification and HAZ-edge boundaries on transverse cross sections of structural steel laser and hybrid laser-GTA welds

### Solidification Boundaries

| WELD 1 | WELD 2 | WELD 3 | WELD 4 |
|---|---|---|---|
| $(y_c$ mm, $z_c$ mm) | $(y_c$ mm, $z_c$ mm) | $(y_c$ mm, $z_c$ mm) | $(y_c$ mm, $z_c$ mm) |
| (5.052, 0.2105) | (7.578, 0.2105) | (5.164, 0.2459) | (5.090, 0.2679) |
| (3.579, 2.105) | (5.894, 1.053) | (3.934, 2.459) | (5.090, 1.340) |
| (2.316, 3.158) | (4.421, 2.105) | (1.967, 4.918) | (4.019, 2.679) |
| (2.316, 4.210) | (3.158, 3.158) | (2.213, 7.377) | (2.947, 4.019) |
| (1.895, 6.315) | (2.316, 4.21) | (1.721, 9.836) | (1.875, 5.358) |
| (1.895, 8.420) | (2.105, 5.263) | (1.721, 12.30) | (1.875, 8.037) |
| (1.684, 10.525) | (1.684, 7.368) | (1.475, 14.75) | (1.607, 10.72) |
| (2.316, 12.0) | (1.684, 9.473) | | (1.875, 12.06) |
| | (1.474, 10.525) | | (1.607, 13.40) |
| | (2.105, 12.0) | | (1.607, 14.73) |

### Solidification Boundaries

| WELD 5 | WELD 6 | WELD 7 | WELD 8 |
|---|---|---|---|
| $(y_c$ mm, $z_c$ mm) | $(y_c$ mm, $z_c$ mm) | $(y_c$ mm, $z_c$ mm) | $(y_c$ mm, $z_c$ mm) |
| (7.501, 0.2679) | (8.773, 0.2830) | (9.793, 0.3159) | (7.938, 0.3175) |
| (6.965, 1.340) | (8.207, 1.415) | (8.529, 1.580) | (7.62, 3.175) |
| (5.894, 2.679) | (6.792, 2.830) | (6.634, 3.159) | (6.668, 4.763) |
| (4.554, 4.019) | (5.377, 4.019) | (4.739, 4.739) | (5.398, 6.35) |
| (2.947, 5.358) | (3.679, 5.66) | (3.159, 6.318) | (4.128, 7.938) |
| (2.411, 6.698) | (2.264, 7.075) | (2.211, 7.898) | (3.81, 9.525) |
| (2.411, 8.037) | (2.264, 8.037) | (2.843, 9.477) | (2.858, 12.7) |
| (2.143, 9.377) | (1.981, 11.32) | (2.843, 11.06) | (2.54, 15.89) |
| (2.143, 10.72) | (1.981, 12.74) | (2.211, 12.64) | (3.175, 19.05) |
| (1.875, 13.40) | (2.264, 14.15) | (1.589, 14.22) | (2.858, 20.0) |
| (1.875, 14.73) | (2.264, 15.0) | (2.211, 15.80) | |
| | | (2.527, 17.37) | |
| | | (2.211, 18.0) | |

### HAZ Edge Boundaries

| WELD 1 | WELD 2 | WELD 3 | WELD 4 |
|---|---|---|---|
| $(y_c$ mm, $z_c$ mm) | $(y_c$ mm, $z_c$ mm) | $(y_c$ mm, $z_c$ mm) | $(y_c$ mm, $z_c$ mm) |
| (6.315, 0.2105) | (9.262, 0.2105) | (7.377, 0.2459) | (7.501, 0.2679) |
| (5.684, 2.105) | (8.42, 1.053) | (6.393, 2.459) | (6.965, 1.340) |
| (5.052, 3.158) | (7.578, 2.105) | (4.918, 4.918) | (6.430, 2.679) |
| (4.21, 4.21) | (6.736, 3.158) | (3.443, 7.377) | (5.626, 4.019) |
| (3.579, 6.315) | (5.473, 4.21) | (3.197, 9.836) | (4.822, 5.358) |
| (3.368, 8.42) | (4.421, 5.263) | (2.705, 12.30) | (3.483, 8.037) |
| (3.158, 10.525) | (3.368, 7.368) | (2.705, 14.75) | (2.947, 10.72) |
| (3.789, 12.0) | (3.158, 9.473) | | (2.947, 12.06) |
| | (3.158, 10.525) | | (2.679, 13.40) |
| | (3.579, 12.0) | | (2.679, 14.73) |

HAZ Edge Boundaries

| WELD 5 | WELD 6 | WELD 7 | WELD 8 |
|---|---|---|---|
| $(y_c \text{ mm}, z_c \text{ mm})$ | $(y_c \text{ mm}, z_c \text{ mm})$ | $(y_c \text{ mm}, z_c \text{ mm})$ | $(y_c \text{ mm}, z_c \text{ mm})$ |
| (10.18, 0.2679) | (10.47, 0.2830) | (12.32, 0.3159) | (12.38, 0.3175) |
| (9.912, 1.340) | (10.47, 1.415) | (11.69, 1.580) | (12.38, 3.175) |
| (9.644, 2.679) | (9.905, 2.830) | (10.11, 3.159) | (11.75, 4.763) |
| (8.573, 4.019) | (9.056, 4.019) | (8.845, 4.739) | (10.80, 6.35) |
| (7.501, 5.358) | (7.924, 5.66) | (6.95, 6.318) | (9.842, 7.938) |
| (5.894, 6.698) | (6.509, 7.075) | (5.686, 7.898) | (8.255, 9.525) |
| (4.554, 8.037) | (5.094, 8.037) | (4.423, 9.477) | (6.35, 12.7) |
| (4.019, 9.377) | (3.962, 11.32) | (4.107, 11.06) | (5.398, 15.89) |
| (3.751, 10.72) | (3.962, 12.74) | (3.475, 12.64) | (5.715, 19.05) |
| (3.483, 13.40) | (3.962, 14.15) | (3.159, 14.22) | (6.033, 20.0) |
| (3.483, 14.73) | (3.962, 15.0) | (3.475, 15.80) | |
| | | (3.791, 17.37) | |
| | | (3.791, 18.0) | |

**Table 2** Volumetric source function $C(\hat{x}_k)$ calculated according to solidification-boundary constraint conditions given in Table 1, where $\Delta l = (12/60)$ mm, $x_k = y_k = 0.0$ for $k = 1$ to $13$ (WELD 1).

| $k$ | $C_k/20.0$ | $z_k \quad (\Delta l)$ |
|---|---|---|
| 1 | 0.23 | 1 |
| 2 | 0.10 | 5 |
| 3 | 0.10 | 10 |
| 4 | 0.07 | 15 |
| 5 | 0.07 | 20 |
| 6 | 0.07 | 25 |
| 7 | 0.07 | 30 |
| 8 | 0.07 | 35 |
| 9 | 0.065 | 40 |
| 10 | 0.065 | 45 |
| 11 | 0.06 | 50 |
| 12 | 0.05 | 55 |
| 13 | 0.05 | 60 |

**Table 3** Volumetric source function $C(\hat{x}_k)$ calculated according to HAZ-edge constraint conditions given in Table 1, where $\Delta l = (12/60)$ mm, $x_k = y_k = 0.0$ for $k = 1$ to $13$ (WELD 1).

| $k$ | $C_k/17.0$ | $z_k \quad (\Delta l)$ |
|---|---|---|
| 1 | 0.18 | 1 |
| 2 | 0.10 | 5 |
| 3 | 0.10 | 10 |
| 4 | 0.07 | 15 |
| 5 | 0.07 | 20 |
| 6 | 0.06 | 25 |
| 7 | 0.06 | 30 |

| 8 | 0.06 | 35 |
|---|---|---|
| 9 | 0.05 | 40 |
| 10 | 0.05 | 45 |
| 11 | 0.05 | 50 |
| 12 | 0.04 | 55 |
| 13 | 0.04 | 60 |

**Table 4** Volumetric source function $C(\hat{x}_k)$ calculated according to solidification-boundary constraint conditions given in Table 1, where $\Delta l = (12/60)$ mm, $x_k = y_k = 0.0$ for $k = 1$ to 13 and $z_k = 1$ for $k = 14$ to 17 (WELD 2).

| $k$ | $C_k/11.5$ | $z_k$ ($\Delta l$) |
|---|---|---|
| 1 | 0.10 | 1 |
| 2 | 0.10 | 5 |
| 3 | 0.10 | 10 |
| 4 | 0.10 | 15 |
| 5 | 0.10 | 20 |
| 6 | 0.10 | 25 |
| 7 | 0.10 | 30 |
| 8 | 0.10 | 35 |
| 9 | 0.10 | 40 |
| 10 | 0.10 | 45 |
| 11 | 0.10 | 50 |
| 12 | 0.06 | 55 |
| 13 | 0.09 | 60 |

| $k$ | $C_k$ | $x_k$ ($\Delta l$) | $y_k$ ($\Delta l$) |
|---|---|---|---|
| 14 | 2.4 | -10.0 | 0.0 |
| 15 | 2.4 | 10.0 | 0.0 |
| 16 | 2.4 | 0.0 | -10.0 |
| 17 | 2.4 | 0.0 | 10.0 |

**Table 5** Volumetric source function $C(\hat{x}_k)$ calculated according to HAZ-edge constraint conditions given in Table 1, where $\Delta l = (12/60)$ mm, $x_k = y_k = 0.0$ for $k = 1$ to 13 and $z_k = 1$ for $k = 14$ to 17 (WELD 2).

| $k$ | $C_k/11.5$ | $z_k$ ($\Delta l$) |
|---|---|---|
| 1 | 0.10 | 1 |
| 2 | 0.10 | 5 |
| 3 | 0.10 | 10 |
| 4 | 0.10 | 15 |
| 5 | 0.10 | 20 |
| 6 | 0.10 | 25 |
| 7 | 0.10 | 30 |
| 8 | 0.10 | 35 |
| 9 | 0.10 | 40 |
| 10 | 0.08 | 45 |
| 11 | 0.07 | 50 |
| 12 | 0.03 | 55 |
| 13 | 0.06 | 60 |

11

| $k$ | $C_k$ | $x_k$ ( $\Delta l$ ) | $y_k$ ( $\Delta l$ ) |
|-----|-------|----------------------|----------------------|
| 14 | 1.5 | -10.0 | 0.0 |
| 15 | 1.5 | 10.0 | 0.0 |
| 16 | 1.5 | 0.0 | -10.0 |
| 17 | 1.5 | 0.0 | 10.0 |

**Table 6** Volumetric source function $C(\hat{x}_k)$ calculated according to solidification-boundary constraint conditions given in Table 1, where $\Delta l = (15/60)$ mm, $x_k = y_k = 0.0$ for $k = 1$ to 13 (WELD 3).

| $k$ | $C_k/15.5$ | $z_k$ ( $\Delta l$ ) |
|-----|------------|----------------------|
| 1 | 0.40 | 1 |
| 2 | 0.10 | 5 |
| 3 | 0.10 | 10 |
| 4 | 0.10 | 15 |
| 5 | 0.10 | 20 |
| 6 | 0.10 | 25 |
| 7 | 0.10 | 30 |
| 8 | 0.10 | 35 |
| 9 | 0.10 | 40 |
| 10 | 0.10 | 45 |
| 11 | 0.08 | 50 |
| 12 | 0.07 | 55 |
| 13 | 0.04 | 60 |

**Table 7** Volumetric source function $C(\hat{x}_k)$ calculated according to HAZ-edge constraint conditions given in Table 1, where $\Delta l = (15/60)$ mm, $x_k = y_k = 0.0$ for $k = 1$ to 13 (WELD 3).

| $k$ | $C_k/14.0$ | $z_k$ ( $\Delta l$ ) |
|-----|------------|----------------------|
| 1 | 0.30 | 1 |
| 2 | 0.10 | 5 |
| 3 | 0.10 | 10 |
| 4 | 0.10 | 15 |
| 5 | 0.10 | 20 |
| 6 | 0.10 | 25 |
| 7 | 0.08 | 30 |
| 8 | 0.08 | 35 |
| 9 | 0.08 | 40 |
| 10 | 0.08 | 45 |
| 11 | 0.07 | 50 |
| 12 | 0.06 | 55 |
| 13 | 0.04 | 60 |

**Table 8** Volumetric source function $C(\hat{x}_k)$ calculated according to solidification-boundary constraint conditions given in Table 1, where $\Delta l = (15/60)$ mm, $x_k = y_k = 0.0$ for $k = 1$ to 13 (WELD 4).

| $k$ | $C_k/15.5$ | $z_k$ $(\Delta l)$ |
|-----|-----------|--------------------|
| 1 | 0.40 | 1 |
| 2 | 0.10 | 5 |
| 3 | 0.10 | 10 |
| 4 | 0.10 | 15 |
| 5 | 0.10 | 20 |
| 6 | 0.10 | 25 |
| 7 | 0.10 | 30 |
| 8 | 0.10 | 35 |
| 9 | 0.10 | 40 |
| 10 | 0.10 | 45 |
| 11 | 0.08 | 50 |
| 12 | 0.08 | 55 |
| 13 | 0.05 | 60 |

**Table 9** Volumetric source function $C(\hat{x}_k)$ calculated according to HAZ-edge constraint conditions given in Table 1, where $\Delta l = (15/60)$ mm, $x_k = y_k = 0.0$ for $k = 1$ to 13 (WELD 4).

| $k$ | $C_k/15.5$ | $z_k$ $(\Delta l)$ |
|-----|-----------|--------------------|
| 1 | 0.30 | 1 |
| 2 | 0.10 | 5 |
| 3 | 0.10 | 10 |
| 4 | 0.10 | 15 |
| 5 | 0.10 | 20 |
| 6 | 0.10 | 25 |
| 7 | 0.08 | 30 |
| 8 | 0.07 | 35 |
| 9 | 0.06 | 40 |
| 10 | 0.06 | 45 |
| 11 | 0.05 | 50 |
| 12 | 0.05 | 55 |
| 13 | 0.04 | 60 |

**Table 10** Volumetric source function $C(\hat{x}_k)$ calculated according to solidification-boundary constraint conditions given in Table 1, where $\Delta l = (15/60)$ mm, $x_k = y_k = 0.0$ for $k = 1$ to 13 (WELD 5).

| $k$ | $C_k/17.5$ | $z_k$ $(\Delta l)$ |
|-----|-----------|--------------------|
| 1 | 0.40 | 1 |
| 2 | 0.30 | 5 |
| 3 | 0.30 | 10 |
| 4 | 0.10 | 15 |
| 5 | 0.10 | 20 |
| 6 | 0.10 | 25 |

13

| 7 | 0.10 | 30 |
|---|---|---|
| 8 | 0.10 | 35 |
| 9 | 0.10 | 40 |
| 10 | 0.10 | 45 |
| 11 | 0.09 | 50 |
| 12 | 0.09 | 55 |
| 13 | 0.05 | 60 |

**Table 11** Volumetric source function $C(\hat{x}_k)$ calculated according to HAZ-edge constraint conditions given in Table 1, where $\Delta l = (15/60)$ mm, $x_k = y_k = 0.0$ for $k = 1$ to 13 (WELD 5).

| $k$ | $C_k/17.5$ | $z_k$ ($\Delta l$) |
|---|---|---|
| 1 | 0.30 | 1 |
| 2 | 0.20 | 5 |
| 3 | 0.20 | 10 |
| 4 | 0.10 | 15 |
| 5 | 0.10 | 20 |
| 6 | 0.10 | 25 |
| 7 | 0.10 | 30 |
| 8 | 0.10 | 35 |
| 9 | 0.07 | 40 |
| 10 | 0.07 | 45 |
| 11 | 0.06 | 50 |
| 12 | 0.05 | 55 |
| 13 | 0.05 | 60 |

**Table 12** Volumetric source function $C(\hat{x}_k)$ calculated according to solidification-boundary constraint conditions given in Table 1, where $\Delta l = (3.0/60)$ mm, $x_k = y_k = 0.0$ for $k = 1$ to 13 (WELD 6).

| $k$ | $C_k/17.5$ | $z_k$ ($\Delta l$) |
|---|---|---|
| 1 | 0.80 | 1 |
| 2 | 0.30 | 5 |
| 3 | 0.30 | 10 |
| 4 | 0.10 | 15 |
| 5 | 0.10 | 20 |
| 6 | 0.10 | 25 |
| 7 | 0.10 | 30 |
| 8 | 0.10 | 35 |
| 9 | 0.10 | 40 |
| 10 | 0.10 | 45 |
| 11 | 0.09 | 50 |
| 12 | 0.09 | 55 |
| 13 | 0.05 | 60 |

**Table 13** Volumetric source function $C(\hat{x}_k)$ calculated according to HAZ-edge constraint conditions given in Table 1, where $\Delta l = (15/60)$ mm, $x_k = y_k = 0.0$ for $k = 1$ to 13 (WELD 6).

| $k$ | $C_k/17.5$ | $z_k$ ($\Delta l$) |
|---|---|---|
| 1 | 0.50 | 1 |
| 2 | 0.20 | 5 |
| 3 | 0.20 | 10 |
| 4 | 0.10 | 15 |
| 5 | 0.10 | 20 |
| 6 | 0.10 | 25 |
| 7 | 0.10 | 30 |
| 8 | 0.10 | 35 |
| 9 | 0.07 | 40 |
| 10 | 0.07 | 45 |
| 11 | 0.06 | 50 |
| 12 | 0.05 | 55 |
| 13 | 0.05 | 60 |

**Table 14** Volumetric source function $C(\hat{x}_k)$ calculated according to solidification-boundary constraint conditions given in Table 1, where $\Delta l = (18/60)$ mm, $x_k = y_k = 0.0$ for $k = 1$ to 13 (WELD 7).

| $k$ | $C_k/17.5$ | $z_k$ ($\Delta l$) |
|---|---|---|
| 1 | 1.00 | 1 |
| 2 | 0.30 | 5 |
| 3 | 0.20 | 10 |
| 4 | 0.10 | 15 |
| 5 | 0.10 | 20 |
| 6 | 0.15 | 25 |
| 7 | 0.15 | 30 |
| 8 | 0.20 | 35 |
| 9 | 0.10 | 40 |
| 10 | 0.10 | 45 |
| 11 | 0.12 | 50 |
| 12 | 0.15 | 55 |
| 13 | 0.05 | 60 |

**Table 15** Volumetric source function $C(\hat{x}_k)$ calculated according to HAZ-edge constraint conditions given in Table 1, where $\Delta l = (18/60)$ mm, $x_k = y_k = 0.0$ for $k = 1$ to 13 (WELD 7).

| $k$ | $C_k/17.5$ | $z_k$ ($\Delta l$) |
|---|---|---|
| 1 | 0.60 | 1 |
| 2 | 0.30 | 5 |
| 3 | 0.20 | 10 |
| 4 | 0.10 | 15 |
| 5 | 0.10 | 20 |
| 6 | 0.10 | 25 |
| 7 | 0.10 | 30 |

| 8 | 0.08 | 35 |
|---|---|---|
| 9 | 0.08 | 40 |
| 10 | 0.08 | 45 |
| 11 | 0.08 | 50 |
| 12 | 0.08 | 55 |
| 13 | 0.05 | 60 |

**Table 16** Volumetric source function $C(\hat{x}_k)$ calculated according to solidification-boundary constraint conditions given in Table 1, where $\Delta l = (20/60)$ mm, $x_k = y_k = 0.0$ for $k = 1$ to 13 (WELD 8).

| $k$ | $C_k/25.0$ | $z_k$ ( $\Delta l$ ) |
|---|---|---|
| 1 | 0.40 | 1 |
| 2 | 0.38 | 5 |
| 3 | 0.35 | 10 |
| 4 | 0.15 | 15 |
| 5 | 0.15 | 20 |
| 6 | 0.15 | 25 |
| 7 | 0.15 | 30 |
| 8 | 0.14 | 35 |
| 9 | 0.12 | 40 |
| 10 | 0.12 | 45 |
| 11 | 0.12 | 50 |
| 12 | 0.12 | 55 |
| 13 | 0.09 | 60 |

**Table 17** Volumetric source function $C(\hat{x}_k)$ calculated according to HAZ-edge constraint conditions given in Table 1, where $\Delta l = (20/60)$ mm, $x_k = y_k = 0.0$ for $k = 1$ to 13 (WELD 8).

| $k$ | $C_k/25.0$ | $z_k$ ( $\Delta l$ ) |
|---|---|---|
| 1 | 0.30 | 1 |
| 2 | 0.29 | 5 |
| 3 | 0.29 | 10 |
| 4 | 0.15 | 15 |
| 5 | 0.15 | 20 |
| 6 | 0.15 | 25 |
| 7 | 0.15 | 30 |
| 8 | 0.14 | 35 |
| 9 | 0.10 | 40 |
| 10 | 0.10 | 45 |
| 11 | 0.10 | 50 |
| 12 | 0.10 | 55 |
| 13 | 0.08 | 60 |
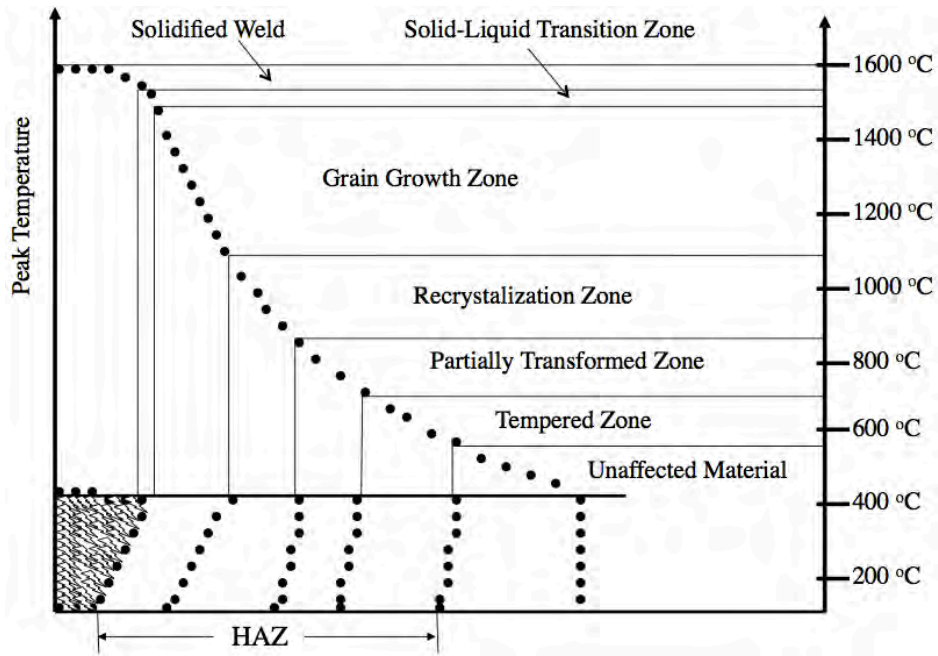
Figure 1. Schematic representation of different regions within the HAZ for steel welds and approximate location of experimentally observable HAZ edge.
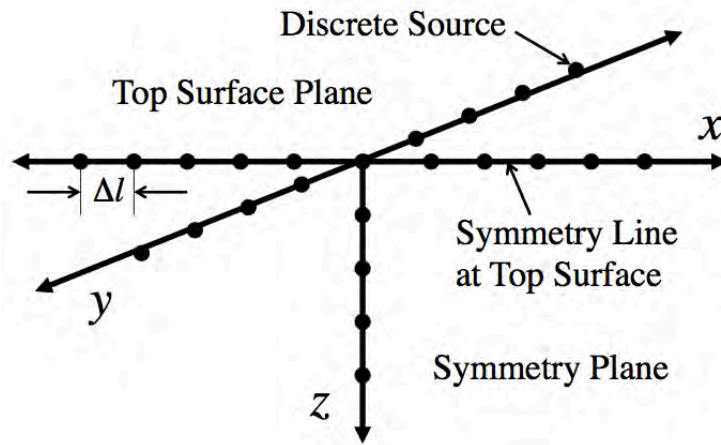


Figure 2. Indexing scheme for relative locations of discrete sources $C(\hat{x}_k)$, $k=1,...,N_k$.
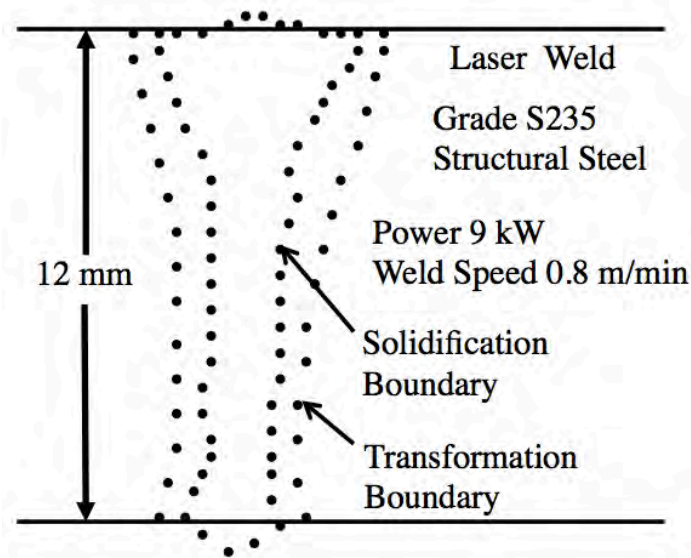
Figure 3. Experimentally measured transverse weld cross sections of solidification and HAZ-edge boundaries for steel laser weld, where V=1.333 cm/s (Weld 1).
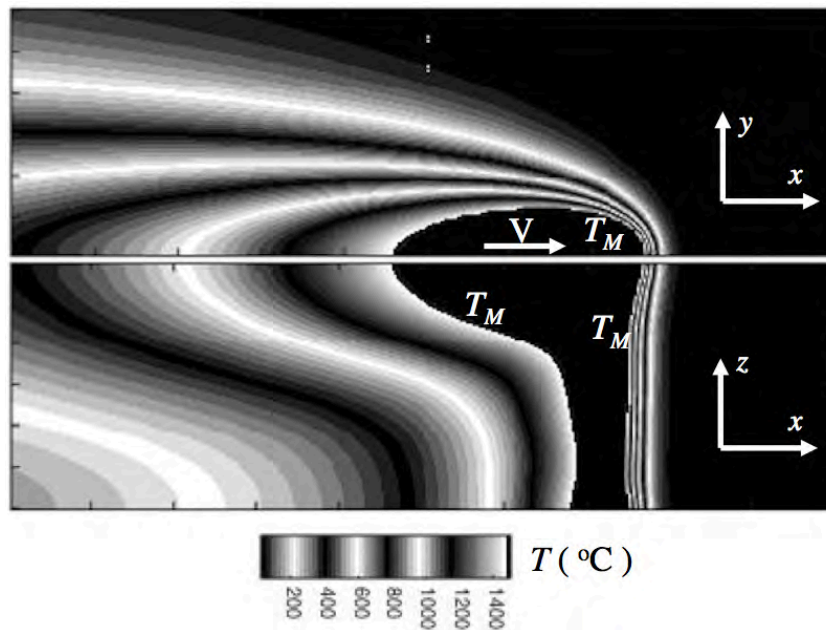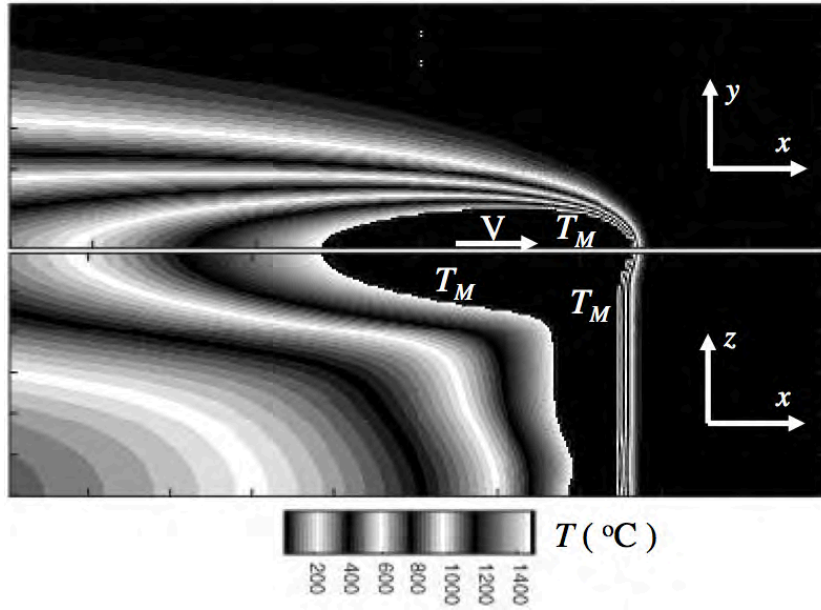


Figure 4. Two-dimensional slices, at half workpiece top surface and longitudinal cross section at symmetry plane, of three-dimensional temperature field (°C) calculated using cross section information given in Table 1 for solidification boundary (Weld 1).
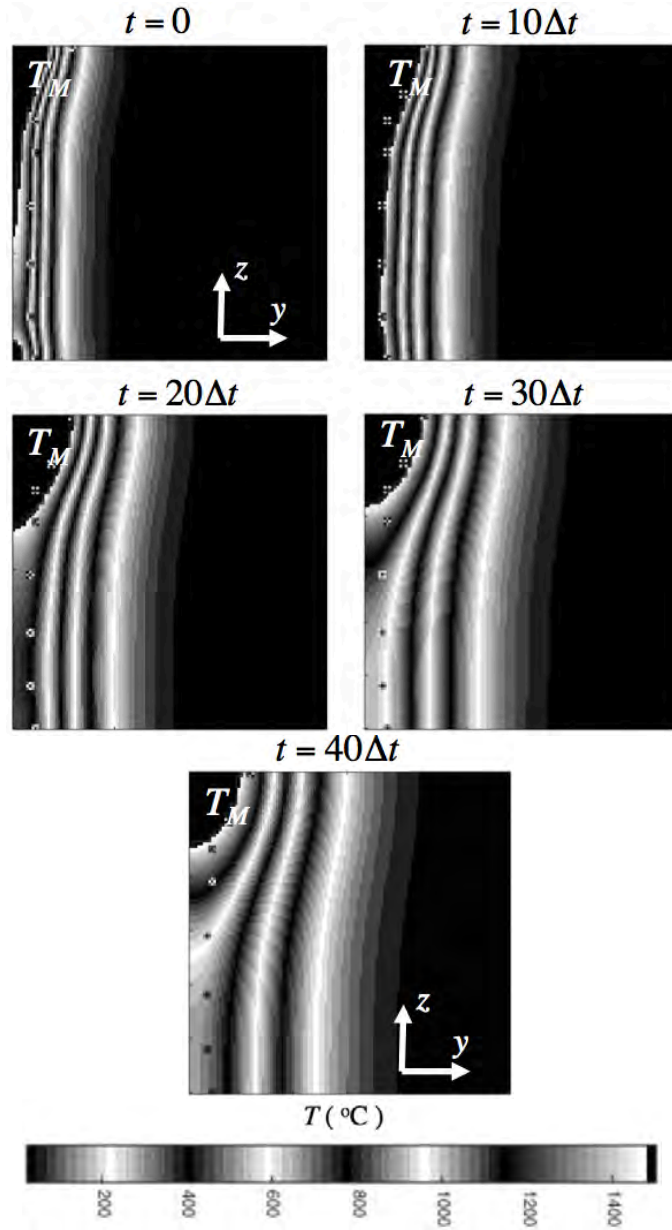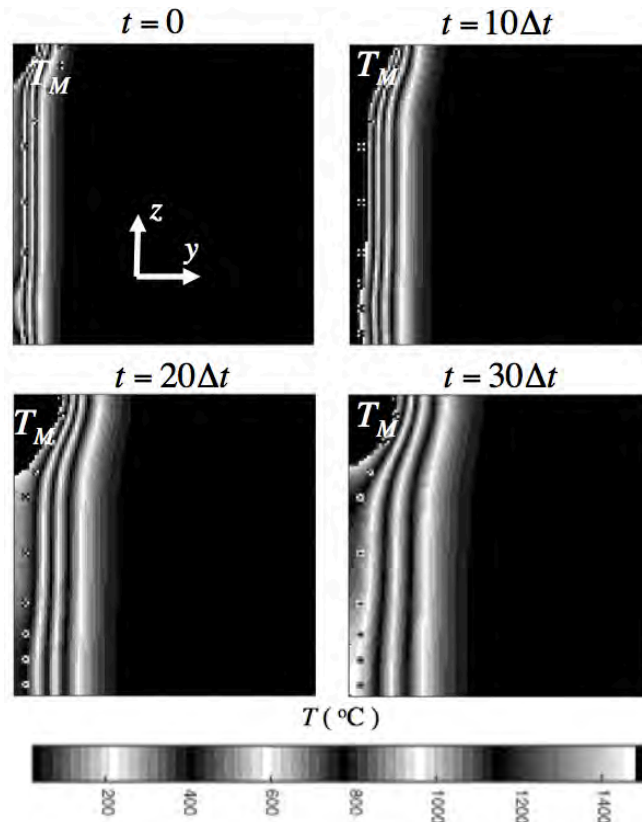
Figure 5. Temperature history ($^{\circ}$C) of transverse cross section of weld calculated using cross section information given in Table 1 for solidification boundary, where $\Delta t = \Delta l / V$, $\Delta l = (12/60)$ mm and V = 1.333 cm/s (Weld 1).
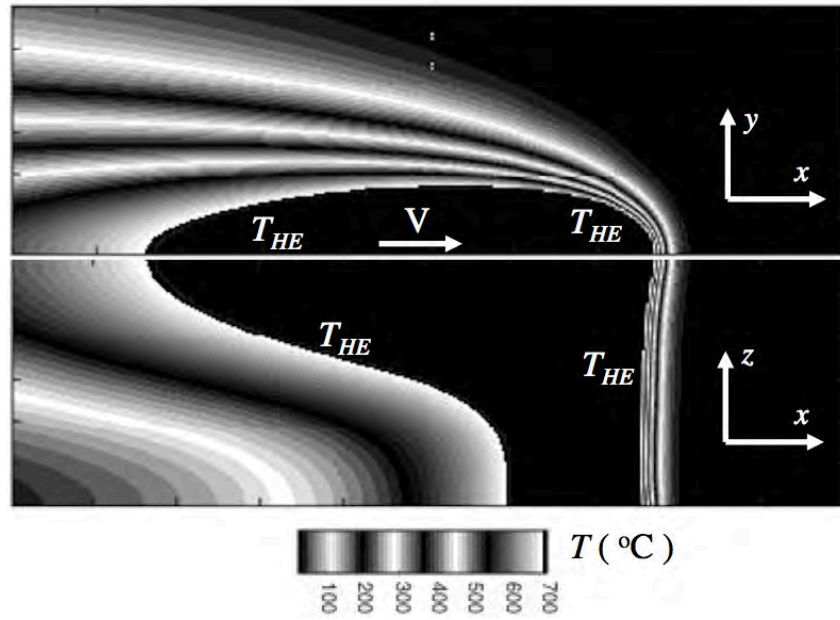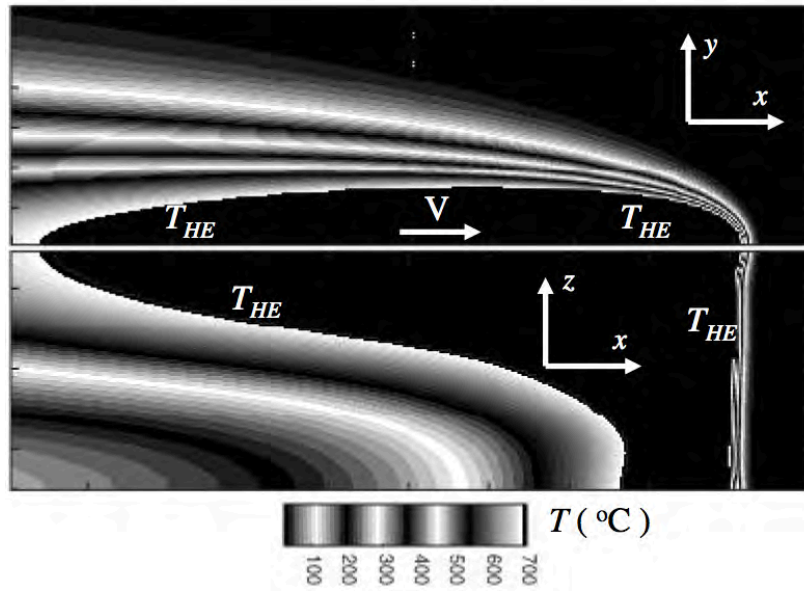
Figure 6. Two-dimensional slices, at half workpiece top surface and longitudinal cross section at symmetry plane, of three-dimensional temperature field ($^{o}$C) calculated using cross section information given in Table 1 for HAZ-edge boundary (Weld 1).
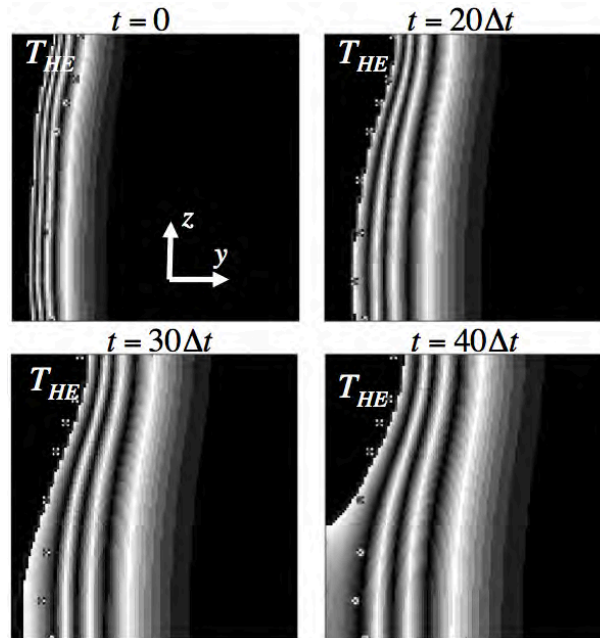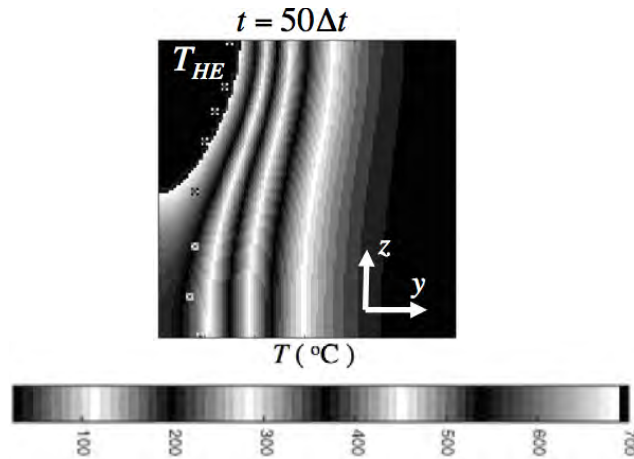
Figure 7. Temperature history ($^{o}$C) of transverse cross section of weld calculated using cross section information given in Table 1 for HAZ-edge boundary, where $\Delta t = \Delta l / V$, $\Delta l = (12/60)$ mm and V = 1.333 cm/s (Weld 1).
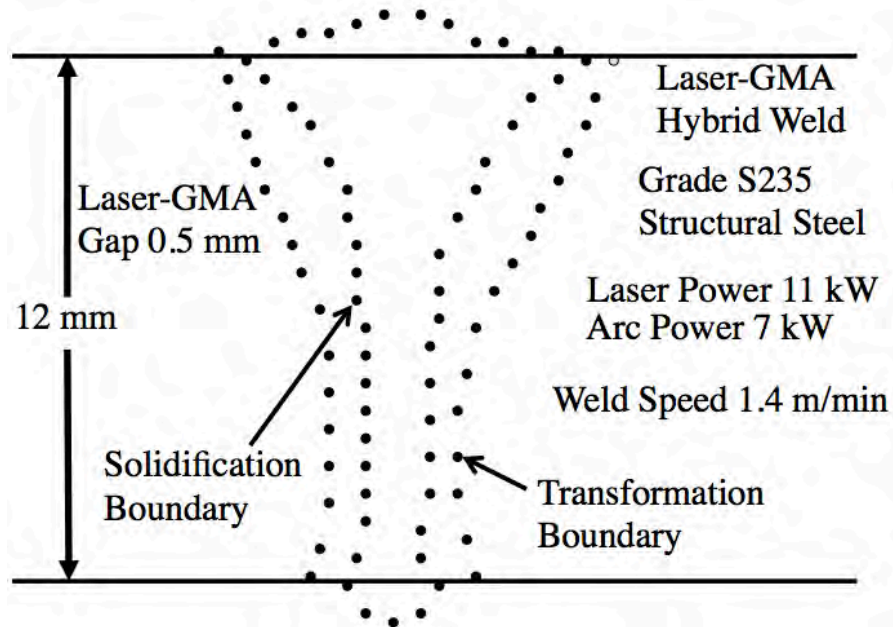


Figure 8. Experimentally measured transverse weld cross sections of solidification and transformation (HAZ-edge) boundaries for steel laser-GMA hybrid weld, where V=2.333 cm/s (Weld 2).
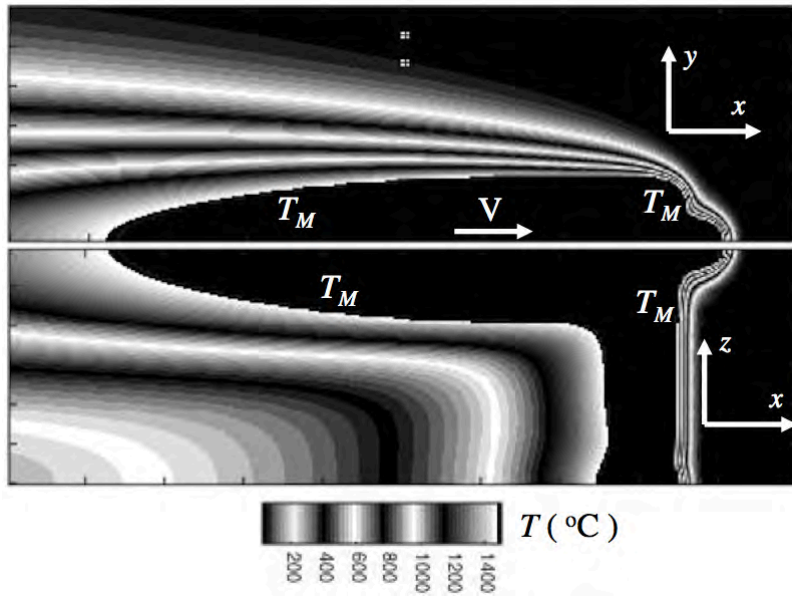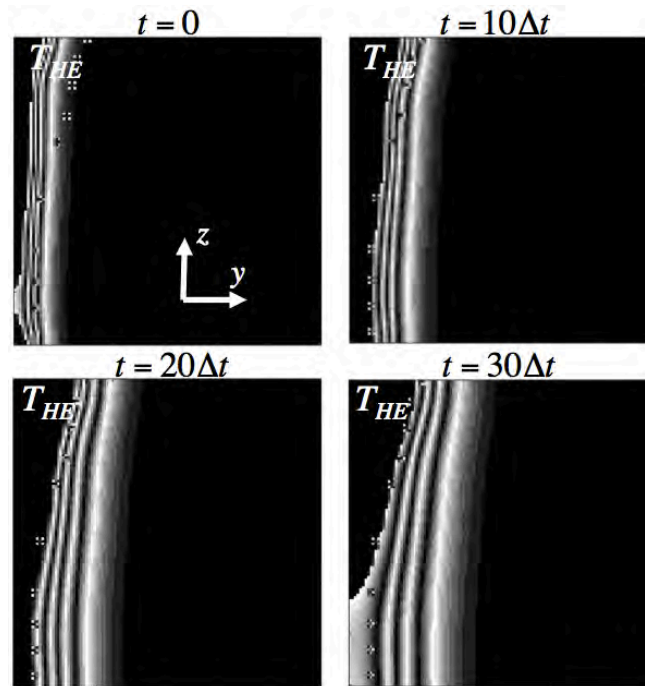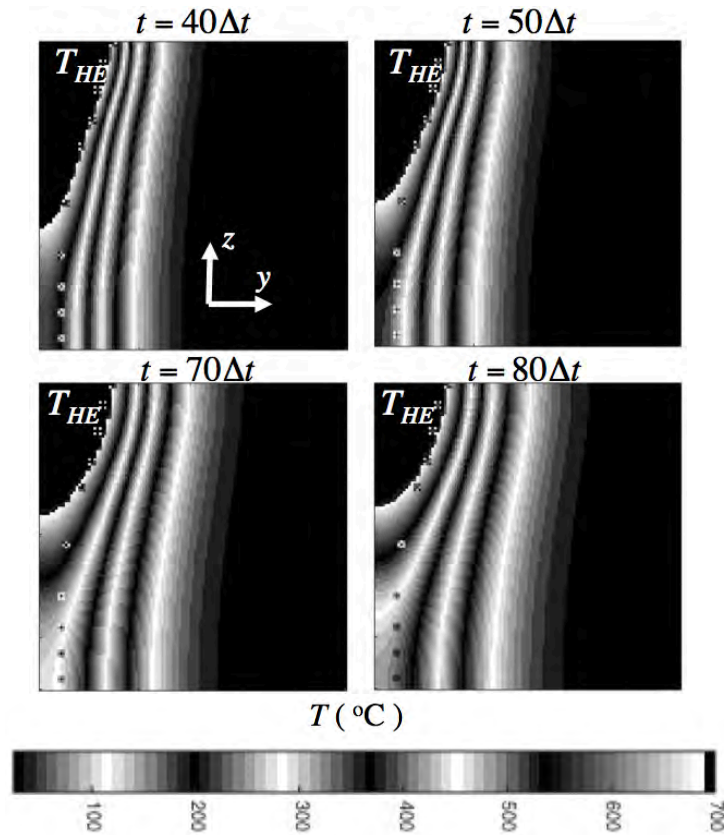
Figure 9. Two-dimensional slices, at half workpiece top surface and longitudinal cross section at symmetry plane, of three-dimensional temperature field ($^{o}$C) calculated using cross section information given in Table 1 for solidification boundary (Weld 2).
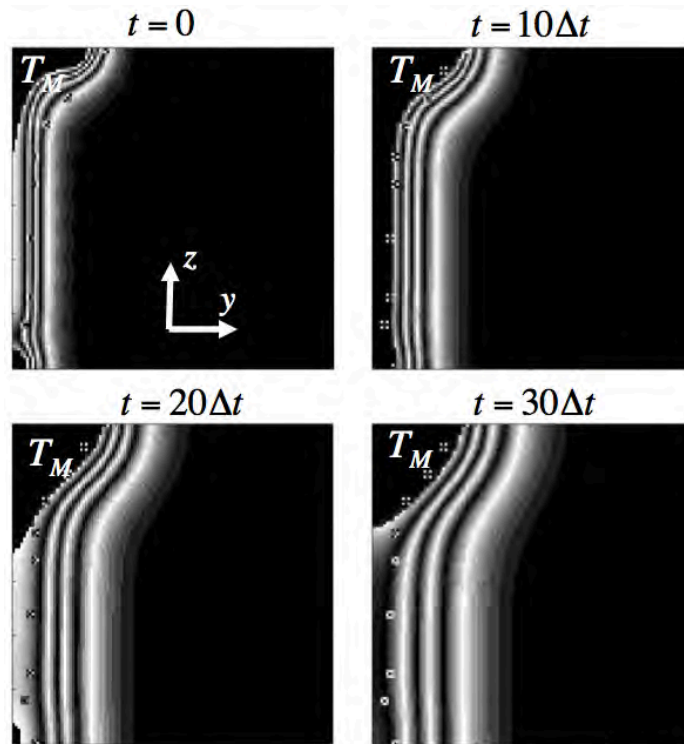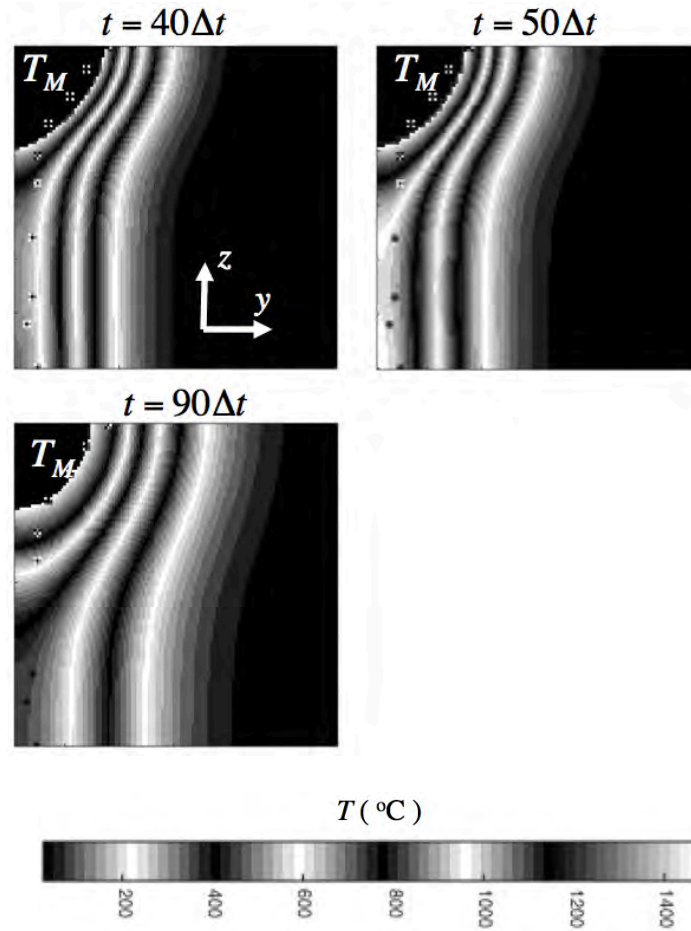
Figure 10. Temperature history ($^{o}$C) of transverse cross section of weld calculated using cross section information given in Table 1 for solidification boundary, where $\Delta t = \Delta l / V$, $\Delta l = (12/60)$ mm and V = 2.333 cm/s (Weld 2).
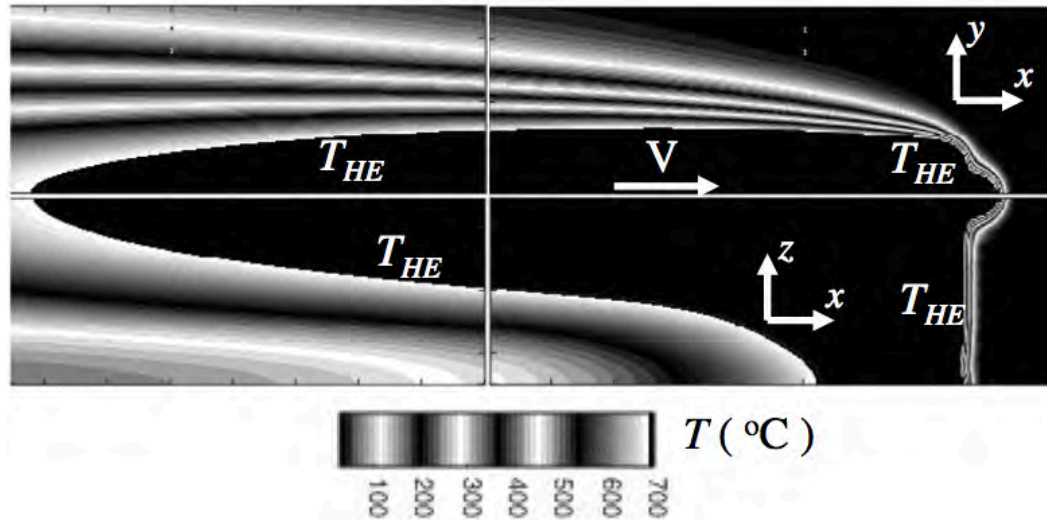


Figure 11. Two-dimensional slices, at half workpiece top surface and longitudinal cross section at symmetry plane, of three-dimensional temperature field ($^{o}$C) calculated using cross section information given in Table 1 for HAZ-edge boundary (Weld 2).
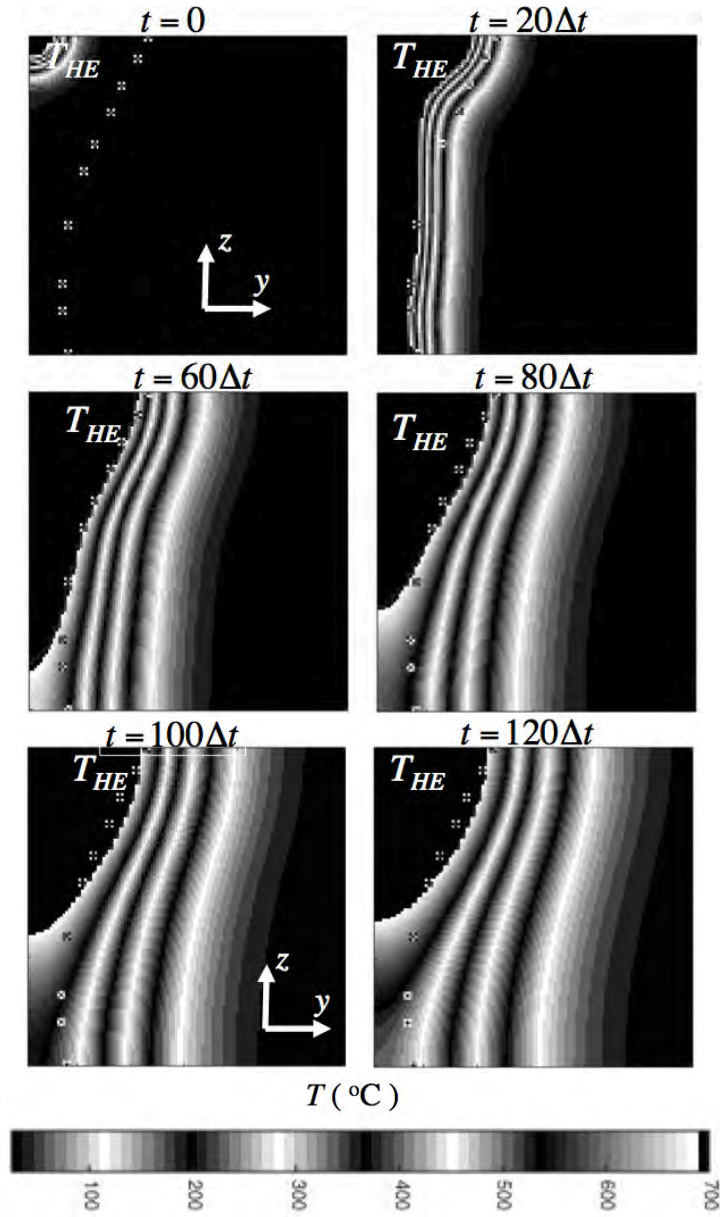
Figure 12. Temperature history ($^o$C) of transverse cross section of weld calculated using cross section information given in Table 1 for HAZ-edge boundary, where $\Delta t = \Delta l / V$, $\Delta l = (12/60)$ mm and V = 2.333 cm/s (Weld 2).
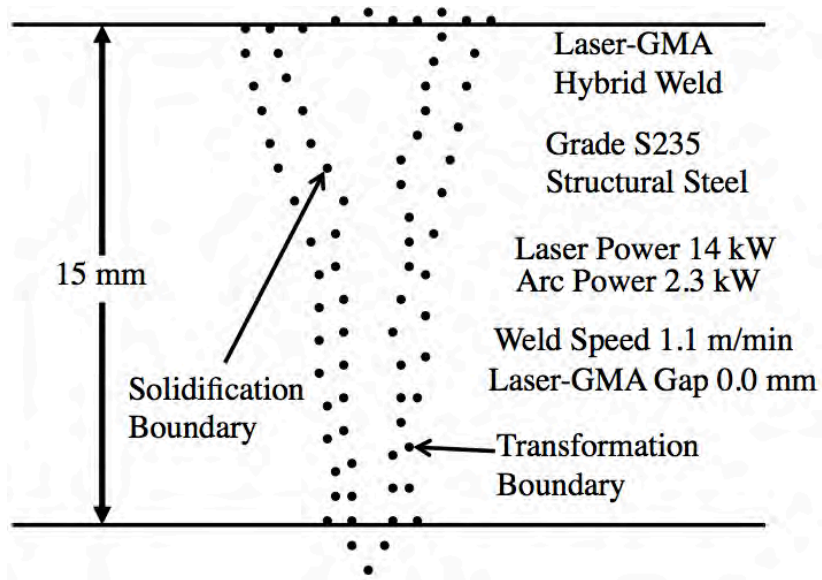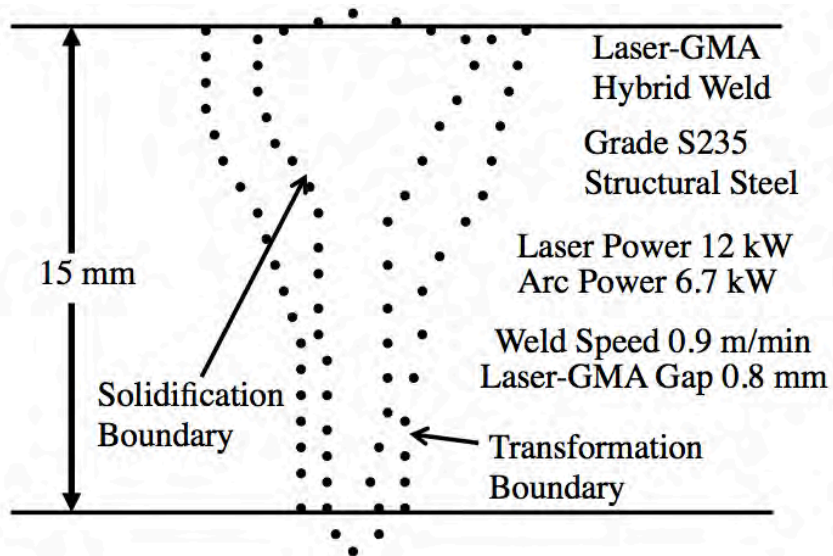
Figure 13. Experimentally measured transverse weld cross sections of solidification and transformation (HAZ-edge) boundaries for steel laser-GMA hybrid weld, where V=1.8333 cm/s (Weld 3).
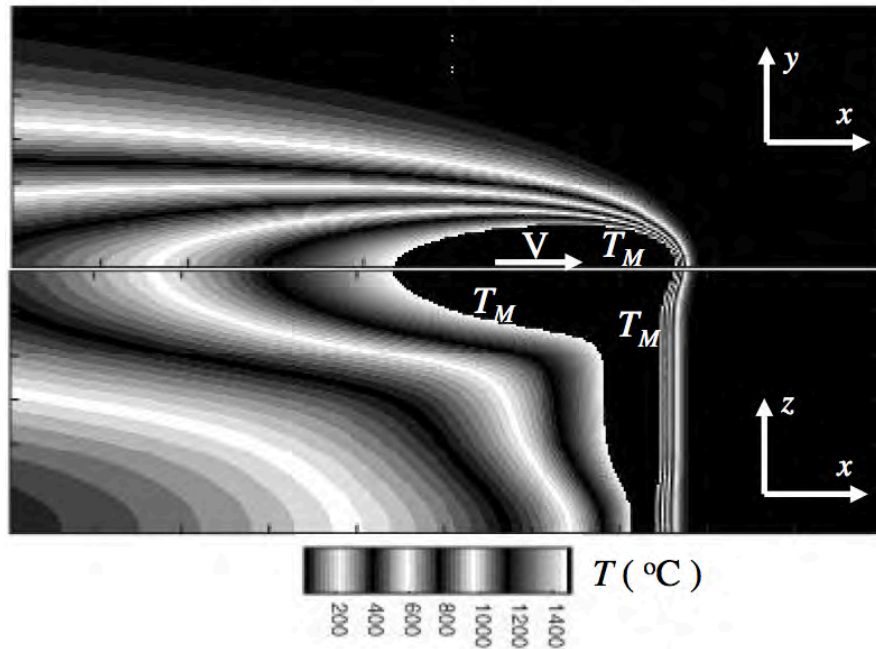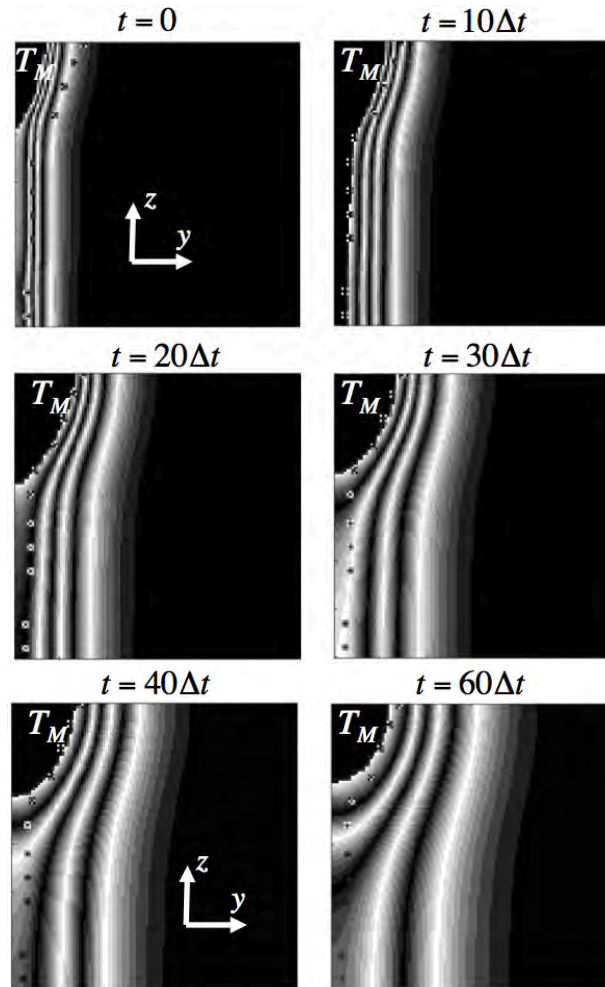


Figure 14. Two-dimensional slices, at half workpiece top surface and longitudinal cross section at symmetry plane, of three-dimensional temperature field ($^{o}$C) calculated using cross section information given in Table 1 for solidification boundary (Weld 3).
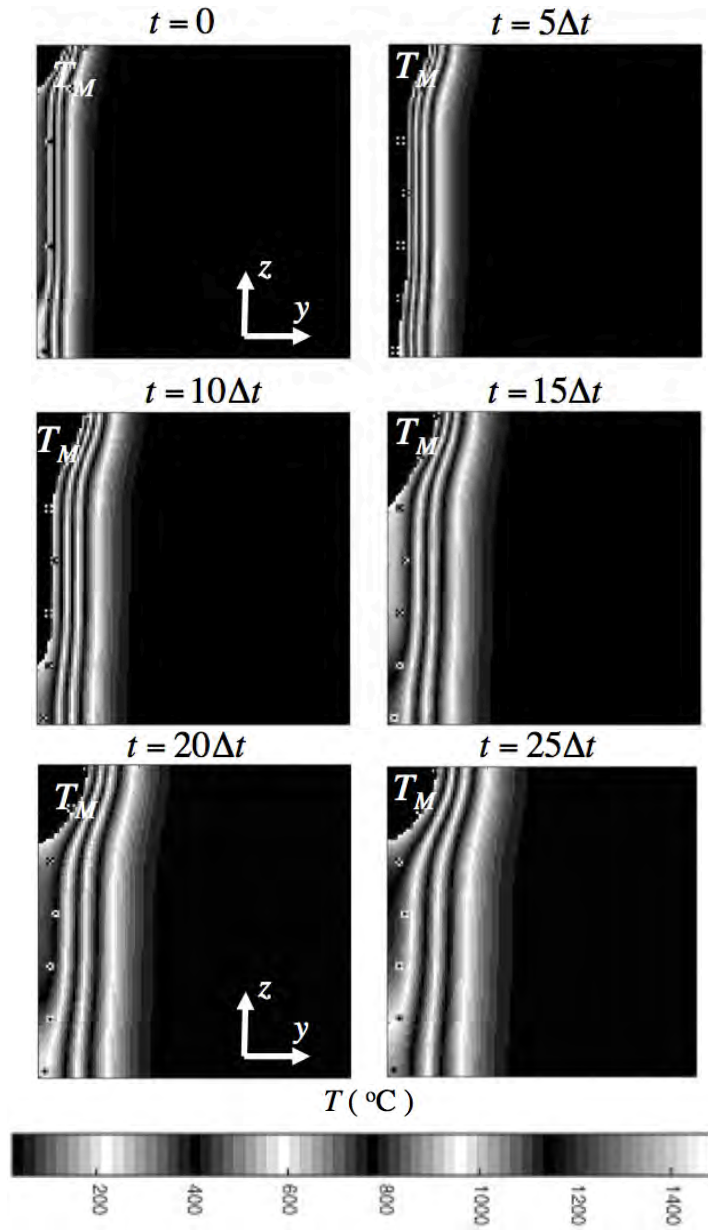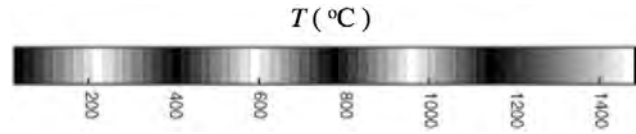
Figure 15. Temperature history ($^{\circ}$C) of transverse cross section of weld calculated using cross section information given in Table 1 for solidification boundary, where $\Delta t = \Delta l / V$, $\Delta l = (15/60)$ mm and V = 1.8333 cm/s (Weld 3).
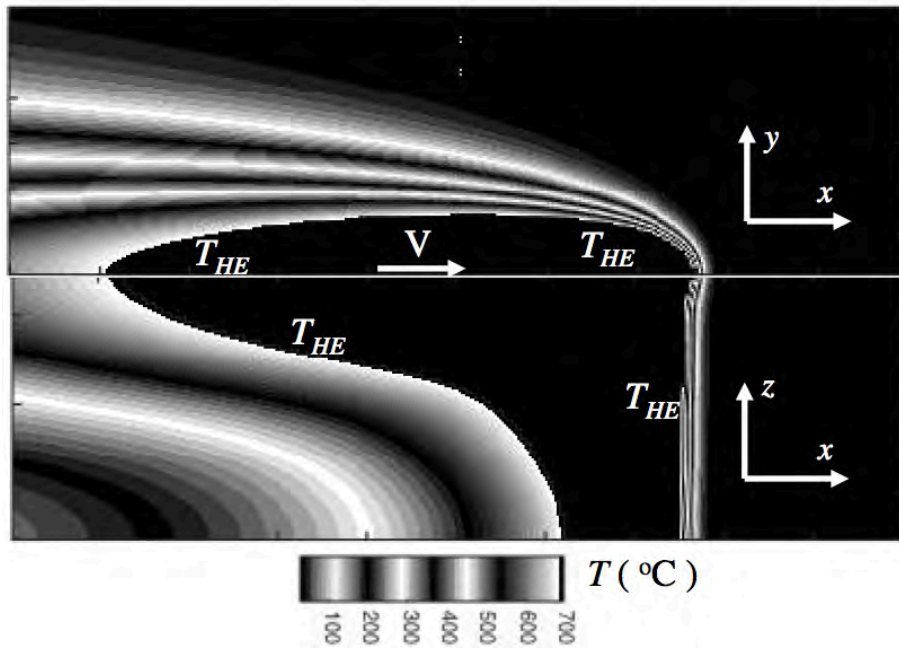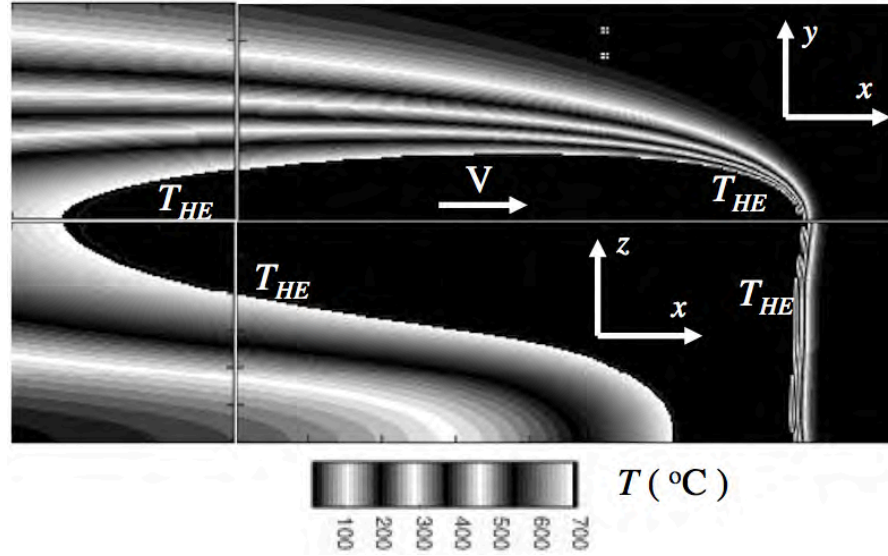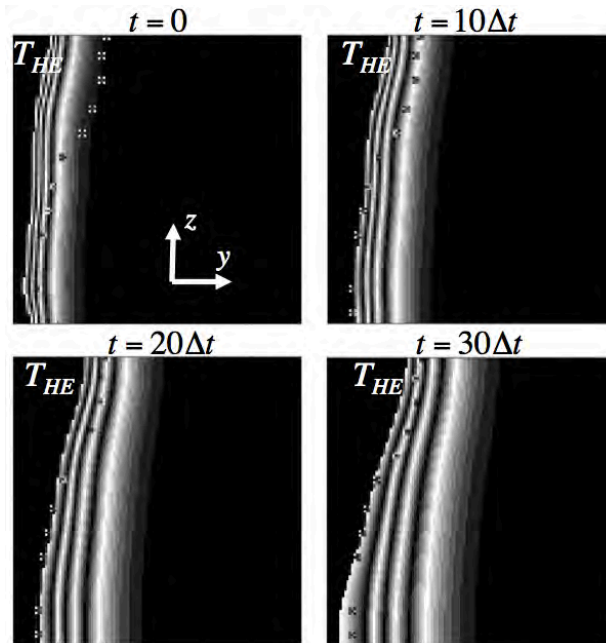
Figure 16. Two-dimensional slices, at half workpiece top surface and longitudinal cross section at symmetry plane, of three-dimensional temperature field ($^{o}$C) calculated using cross section information given in Table 1 for HAZ-edge boundary (Weld 3).
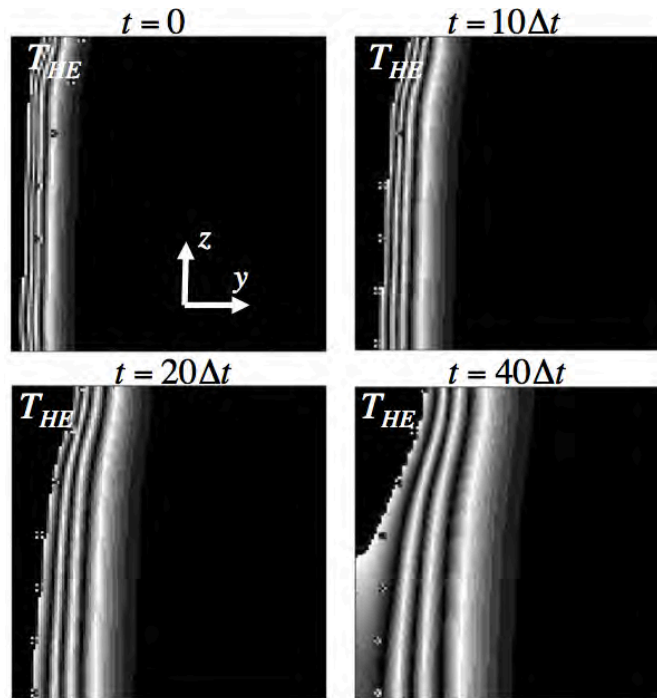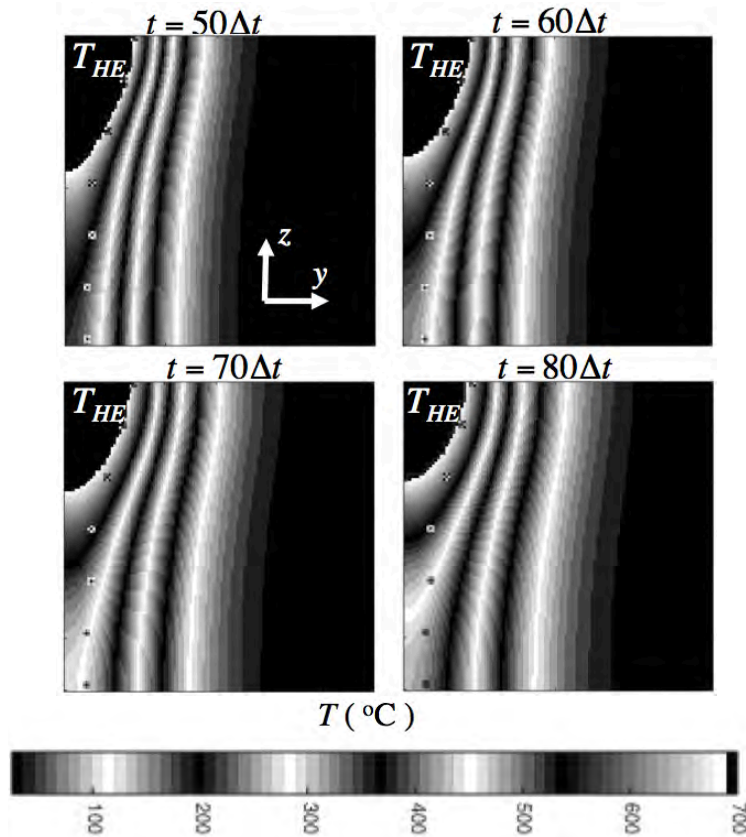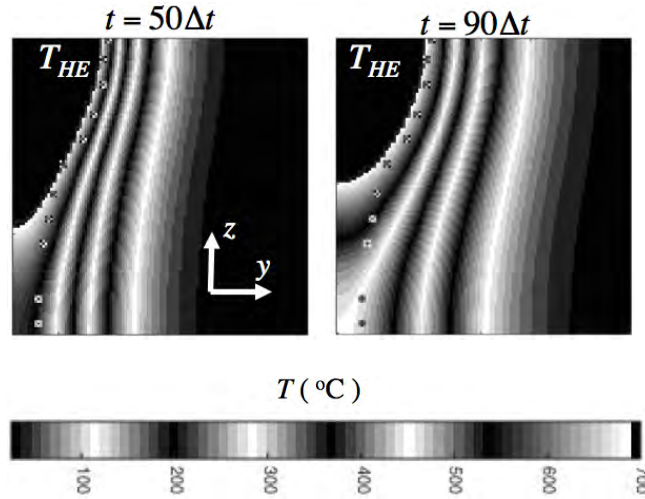
Figure 17. Temperature history ($^{\mathrm{o}}$C) of transverse cross section of weld calculated using cross section information given in Table 1 for HAZ-edge boundary, where $\Delta t = \Delta l / V$, $\Delta l = (15/60)$ mm and V = 1.8333 cm/s (Weld 3).
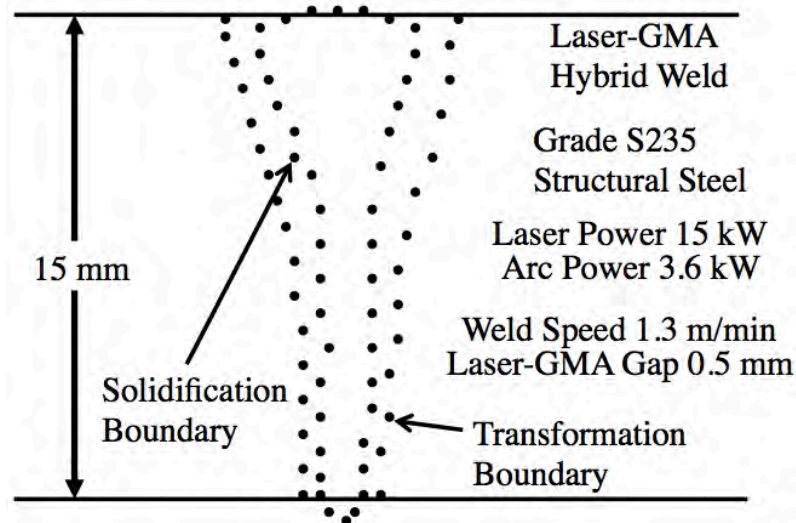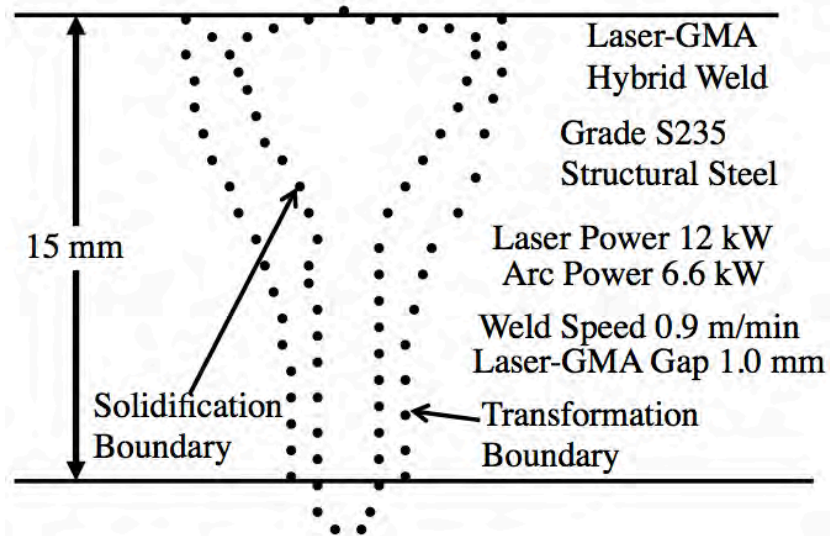


Figure 18. Experimentally measured transverse weld cross sections of solidification and transformation (HAZ-edge) boundaries for steel laser-GMA hybrid weld, where V=2.1666 cm/s (Weld 4).

Figure 19. Two-dimensional slices, at half workpiece top surface and longitudinal cross section at symmetry plane, of three-dimensional temperature field ($^{o}$C) calculated using cross section information given in Table 1 for solidification boundary (Weld 4).



Figure 20. Temperature history ($^{o}$C) of transverse cross section of weld calculated using cross section information given in Table 1 for solidification boundary, where $\Delta t = \Delta l / V$, $\Delta l = (15/60)$ mm and $V = 2.1666$ cm/s (Weld 4).
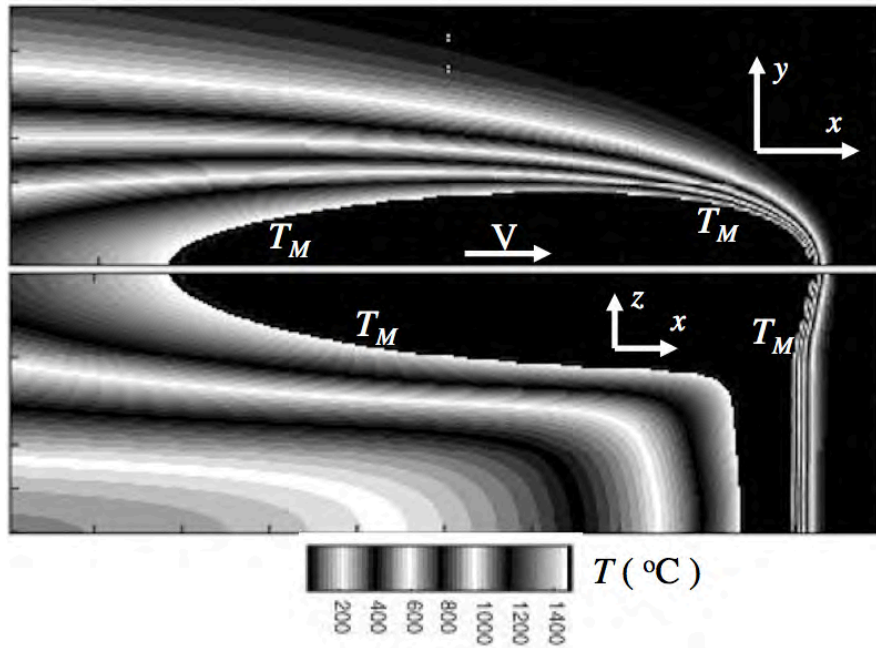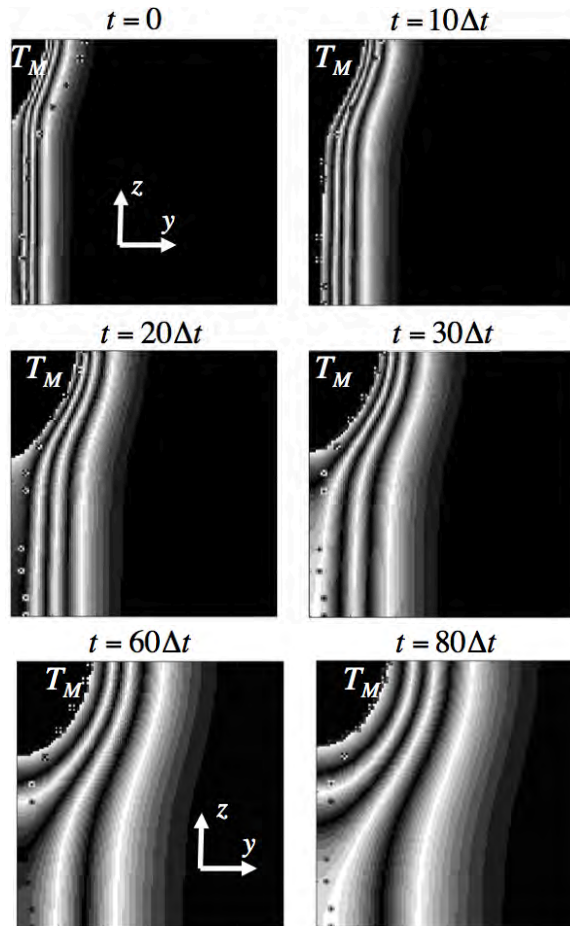
Figure 21. Two-dimensional slices, at half workpiece top surface and longitudinal cross section at symmetry plane, of three-dimensional temperature field ($^{o}$C) calculated using cross section information given in Table 1 for HAZ-edge boundary (Weld 4).

Figure 22. Temperature history ($^o$C) of transverse cross section of weld calculated using cross section information given in Table 1 for HAZ-edge boundary, where $\Delta t = \Delta l / V$, $\Delta l = (15/60)$ mm and V = 2.1666 cm/s (Weld 4).



Figure 23. Experimentally measured transverse weld cross sections of solidification and transformation (HAZ-edge) boundaries for steel laser-GMA hybrid weld, where V=1.5 cm/s (Weld 5).

31
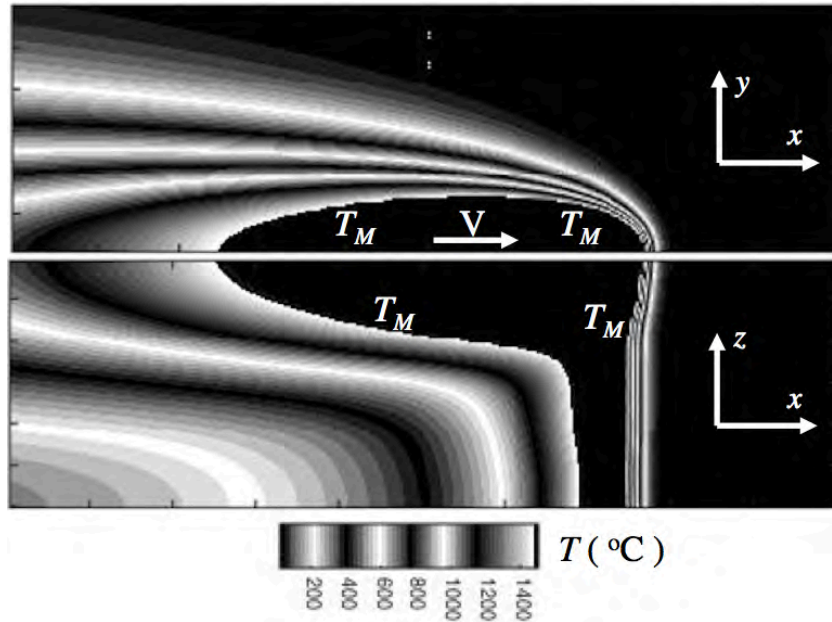
Figure 24. Two-dimensional slices, at half workpiece top surface and longitudinal cross section at symmetry plane, of three-dimensional temperature field (°C) calculated using cross section information given in Table 1 for solidification boundary (Weld 5).

$T(^oC)$

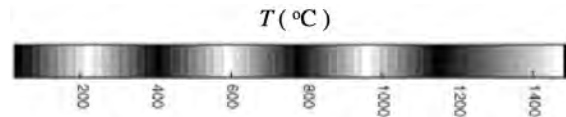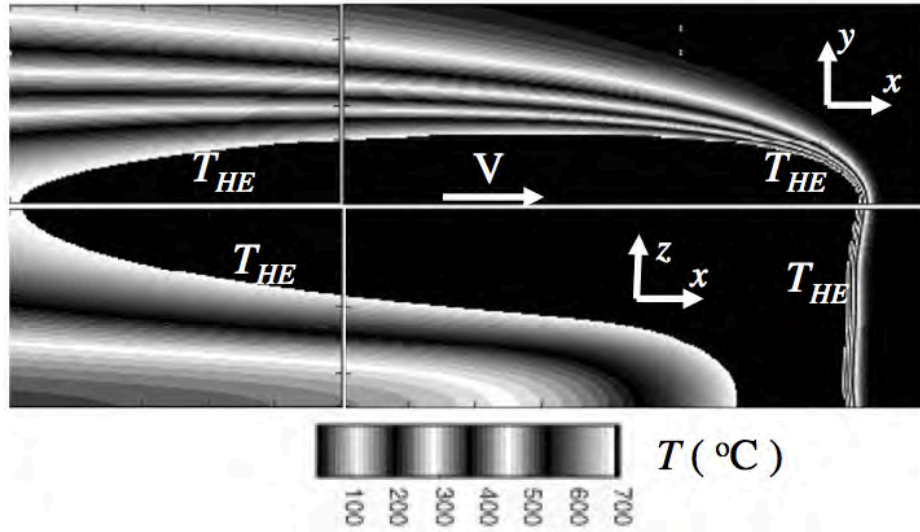Figure 25. Temperature history ($^o$C) of transverse cross section of weld calculated using cross section information given in Table 1 for solidification boundary, where $\Delta t = \Delta l / V$, $\Delta l = (15/60)$ mm and V = 1.5 cm/s (Weld 5).
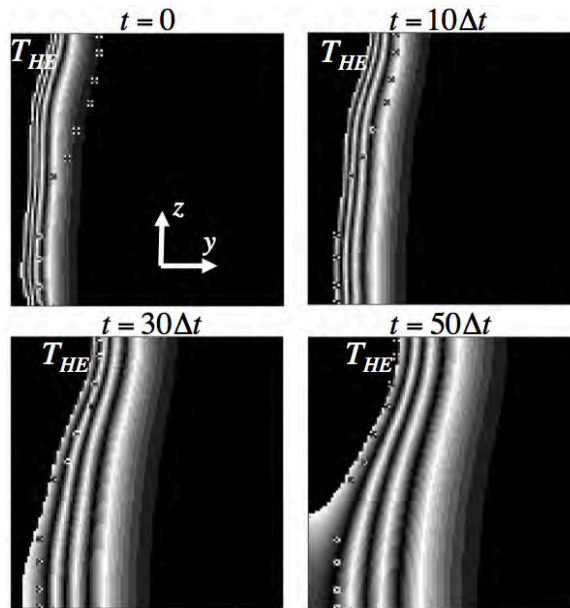


$T(^oC)$

Figure 26. Two-dimensional slices, at half workpiece top surface and longitudinal cross section at symmetry plane, of three-dimensional temperature field ($^o$C) calculated using cross section information given in Table 1 for HAZ-edge boundary (Weld 5).
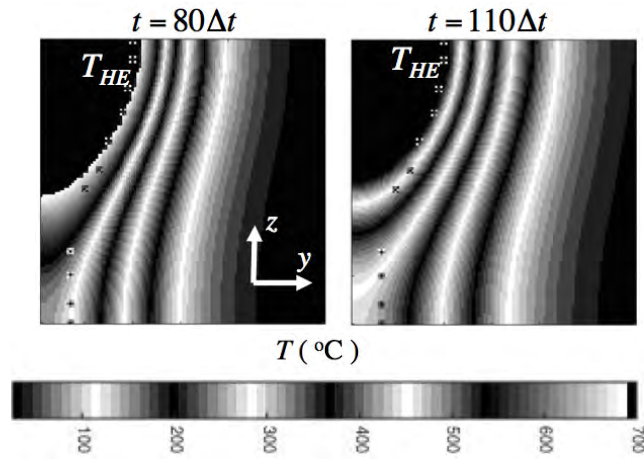


33

Figure 27. Temperature history (°C) of transverse cross section of weld calculated using cross section information given in Table 1 for HAZ-edge boundary, where $\Delta t = \Delta l /V$, $\Delta l = (15/60)$ mm and V = 1.5 cm/s (Weld 5).
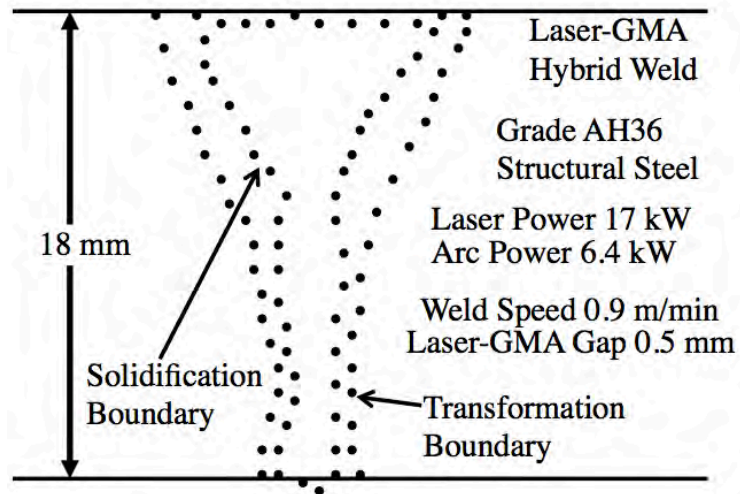


Figure 28. Experimentally measured transverse weld cross sections of solidification and transformation (HAZ-edge) boundaries for steel laser-GMA hybrid weld, where V=1.5 cm/s (Weld 6).
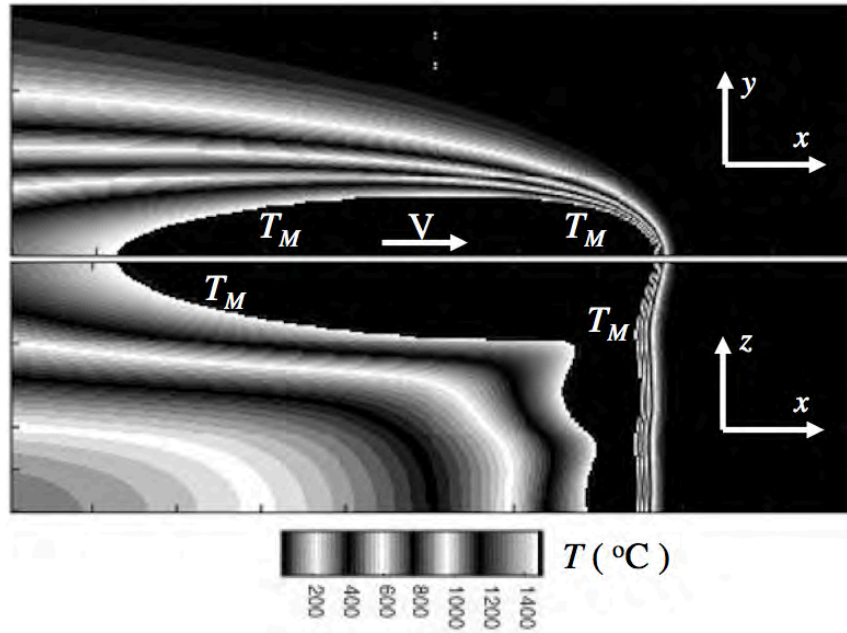
Figure 29. Two-dimensional slices, at half workpiece top surface and longitudinal cross section at symmetry plane, of three-dimensional temperature field ($^{o}$C) calculated using cross section information given in Table 1 for solidification boundary (Weld 6).
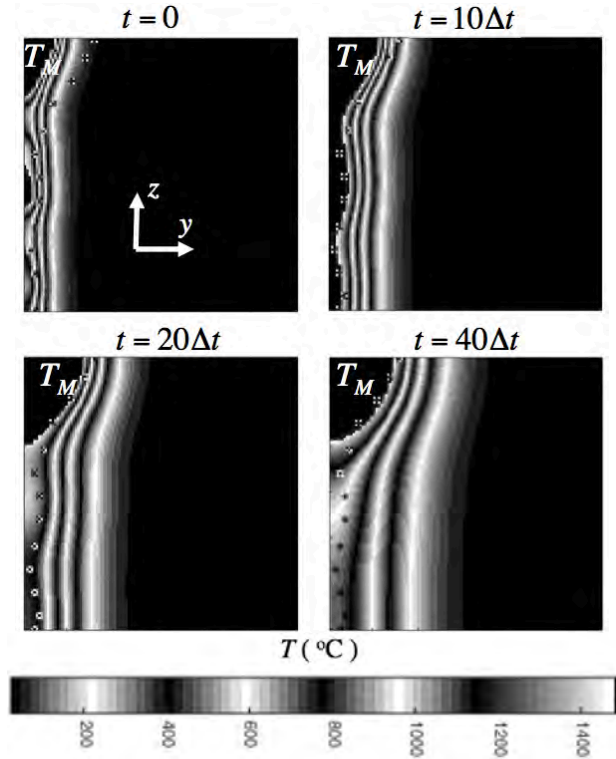
Figure 30. Temperature history ($^o$C) of transverse cross section of weld calculated using cross section information given in Table 1 for solidification boundary, where $\Delta t = \Delta l /V$, $\Delta l = (15/60)$ mm and V = 1.5 cm/s (Weld 6).



Figure 31. Two-dimensional slices, at half workpiece top surface and longitudinal cross section at symmetry plane, of three-dimensional temperature field ($^o$C) calculated using cross section information given in Table 1 for HAZ-edge boundary (Weld 6).

Figure 32. Temperature history (°C) of transverse cross section of weld calculated using cross section information given in Table 1 for HAZ-edge boundary, where $\Delta t = \Delta l / V$, $\Delta l = (15/60)$ mm and V = 1.5 cm/s (Weld 6).



Figure 33. Experimentally measured transverse weld cross sections of solidification and transformation (HAZ-edge) boundaries for steel laser-GMA hybrid weld, where V=1.5 cm/s (Weld 7).
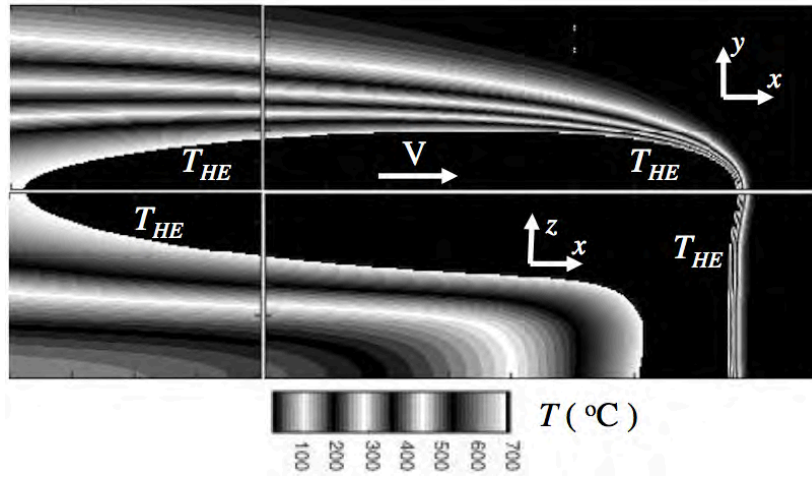
Figure 34. Two-dimensional slices, at half workpiece top surface and longitudinal cross section at symmetry plane, of three-dimensional temperature field ($^{o}$C) calculated using cross section information given in Table 1 for solidification boundary (Weld 7).



Figure 35. Temperature history ($^{o}$C) of transverse cross section of weld calculated using cross section information given in Table 1 for solidification boundary, where $\Delta t = \Delta l / V$, $\Delta l = (18/60)$ mm and $V = 1.5$ cm/s (Weld 7).

Figure 36. Two-dimensional slices, at half workpiece top surface and longitudinal cross section at symmetry plane, of three-dimensional temperature field ($^{\circ}$C) calculated using cross section information given in Table 1 for HAZ-edge boundary (Weld 7).
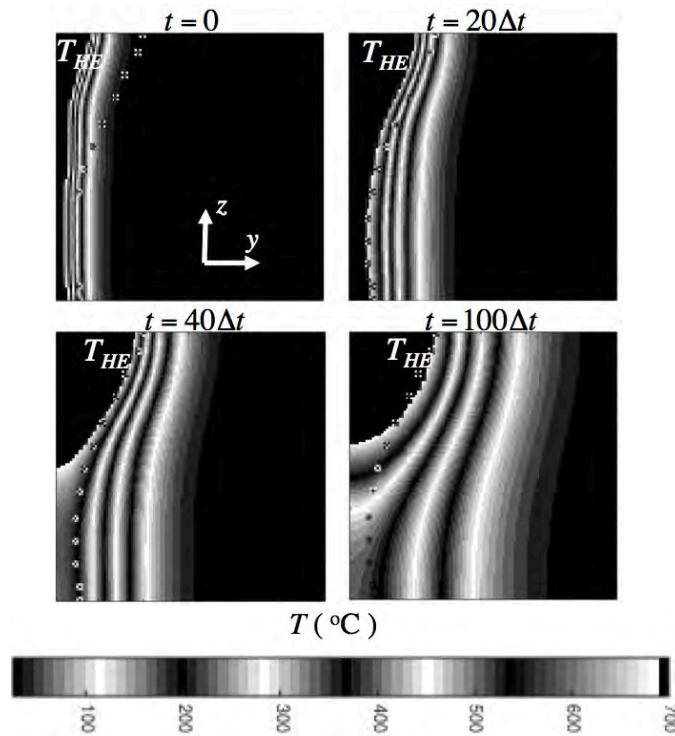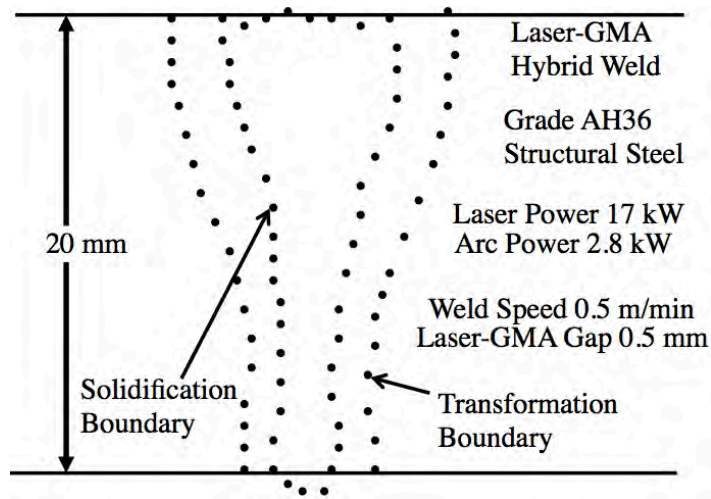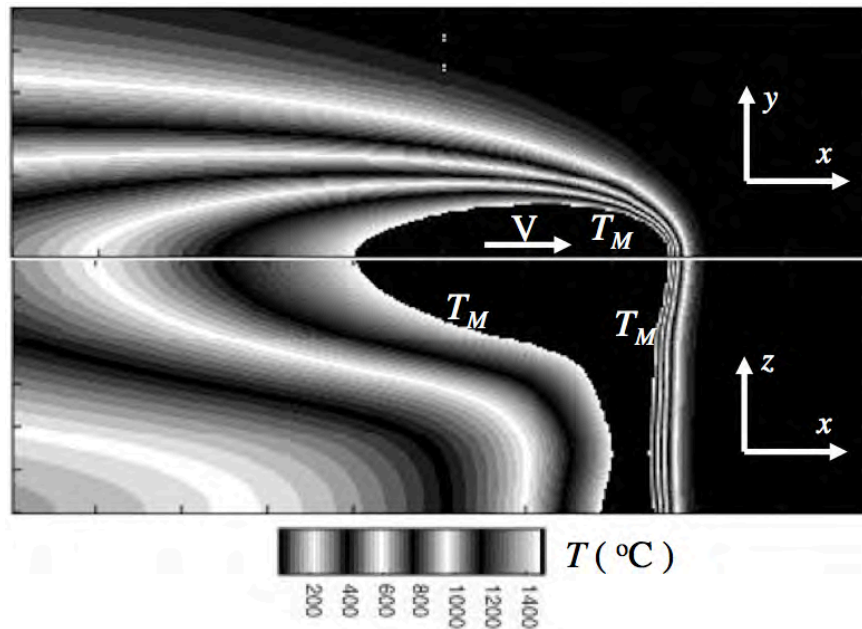


Figure 37. Temperature history ($^{\circ}$C) of transverse cross section of weld calculated using cross section information given in Table 1 for HAZ-edge boundary, where $\Delta t = \Delta l / V$, $\Delta l = (20/60)$ mm and V = 1.5 cm/s (Weld 7).

Figure 38. Experimentally measured transverse weld cross sections of solidification and transformation (HAZ-edge) boundaries for steel laser-GMA hybrid weld, where V=8.333 mm/s (Weld 8).



Figure 39. Two-dimensional slices, at half workpiece top surface and longitudinal cross section at symmetry plane, of three-dimensional temperature field (°C) calculated using cross section information given in Table 1 for solidification boundary (Weld 8).
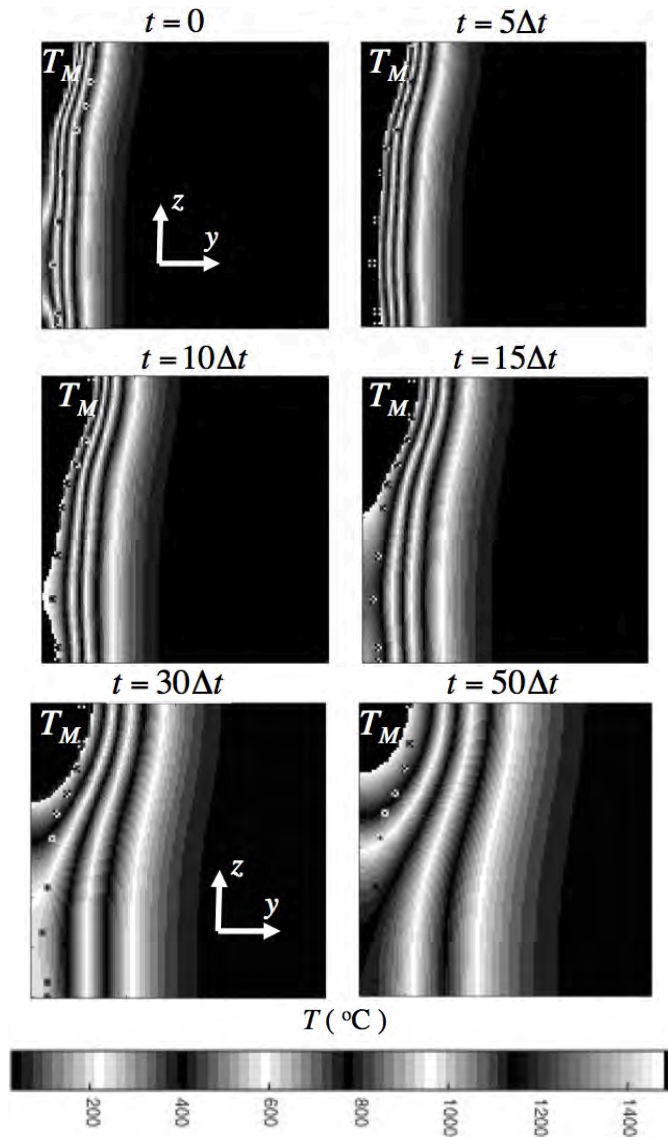
Figure 40. Temperature history ($^{\circ}$C) of transverse cross section of weld calculated using cross section information given in Table 1 for solidification boundary, where $\Delta t = \Delta l / V$, $\Delta l = (20/60)$ mm and V = 8.333 mm/s (Weld 8).
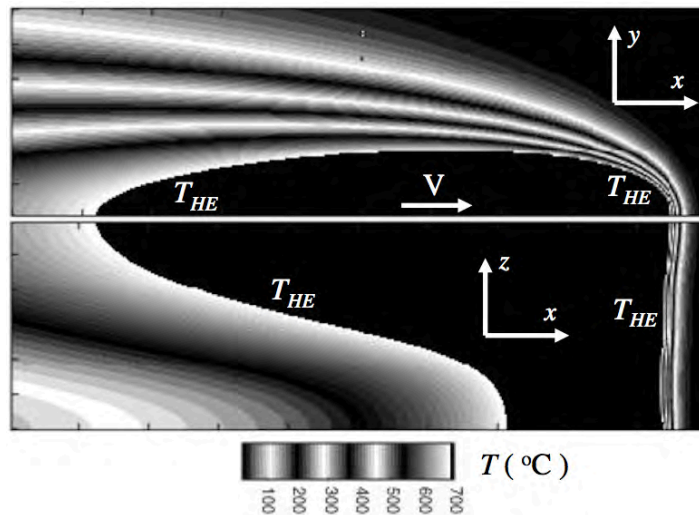
Figure 41. Two-dimensional slices, at half workpiece top surface and longitudinal cross section at symmetry plane, of three-dimensional temperature field ($^{o}$C) calculated using cross section information given in Table 1 for HAZ-edge boundary (Weld 8).
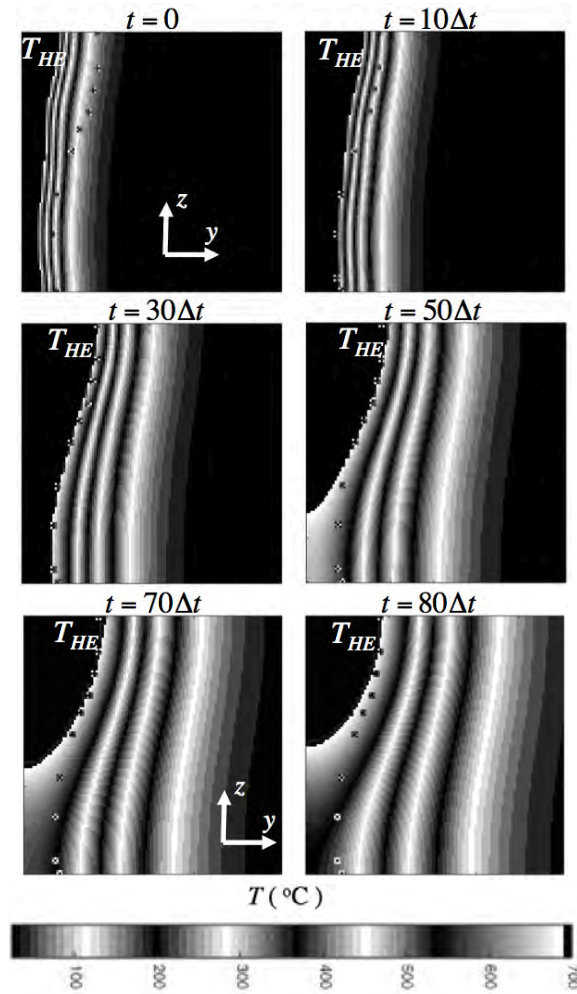


Figure 42. Temperature history ($^{o}$C) of transverse cross section of weld calculated using cross section information given in Table 1 for HAZ-edge boundary, where $\Delta t = \Delta l / V$, $\Delta l = (20/60)$ mm and V = 8.333 mm/s (Weld 8).